Redox control of chromium in the red soils from China evidenced by Cr stable isotopes

Xiaoquan Qin, Damien Guinoiseau, Zongling Ren, Marc F Benedetti

Redox control of chromium in the red soils from China evidenced by Cr stable isotopes

Xiaoquan Qin[1], Damien Guinoiseau[2], Zongling Ren[3] and Marc F. Benedetti[1]

1 Université Paris Cité – Institut de Physique du globe de Paris, CNRS, F75005 Paris, France

2 Université Paris Saclay, CNRS, UMR8148 GEOPS, 91400 Orsay, France

3 Department of Soil Science, College of Natural Resources and Environment, South China Agricultural University, Guangzhou 510642, China

Highlights

- Cr isotope data in soil FMNs is reported for the first time.
- FMNs/Fe oxides capture isotopically heavy Cr (VI).
- Redox and not land use drives Fe oxide formation and FMNs, affecting Cr mobility.
- Cr in red soil profiles mainly results from colluvium mineral weathering.

Abstract

With chromium isotopes, we study the intricate dynamics of adsorption and redox processes in soil ecosystems, focusing on chromium's behaviour, in red soil profiles enriched with iron-manganese nodules (FMNs) in South China. Key findings reveal that the primary geological source of chromium in the red soil profiles is the weathering of colluvium parent minerals. FMNs have higher chromium concentrations (325-1,451 µg/g) compared to surrounding soils (95-247 µg/g) and display stable δ^{53}Cr values (0.78 ± 0.17‰), indicating their role as stable chromium repositories, reflecting historical processes. Furthermore, by isolating chromium associated with iron oxides (FeO) and silicate minerals (ReS) within FMNs and surrounding soils using CBD extractions, we show that FeO predominantly carry chromium, particularly in FMNs. The δ^{53}Cr values of FeO fractions consistently exhibit heavier

signatures than ReS fractions, suggesting the sequestration of isotopically heavy chromium (VI) during Fe oxide precipitation. Fluctuations in soil's redox, rather than land use, play a pivotal role in controlling the precipitation of Fe oxides in surrounding soils and the formation of FMNs, thus influencing chromium mobility. This highlights the significance of these factors when utilizing chromium isotopic techniques for source tracking in soil systems, contributing to our understanding of chromium's behaviour in soil environments.

Keywords

Chromium hazard, Chromium isotopes, red soil, iron-manganese nodules, soil redox, Iron oxides

1. Introduction

In soils, stable Cr is found as trivalent (III) and hexavalent (VI) species with low concentrations (15-100 μg/g) in general (Shahid et al., 2017). However, high Cr levels (180-60,000 μg/g) can be measured in soils developed over mafic and ultramafic rocks like serpentinite or basalt (Fandeur et al., 2009; Paulukat et al., 2015; Sun et al., 2022). Anthropogenic activities, such as mining, smelting, paper and leather manufacturing, result in ~2.3 $Mg \cdot yr^{-1}$ of chromium flux into soils and are the major contributors to soil chromium contamination (Rauch and Pacyna, 2009). Therefore, soil Cr contamination is becoming a widespread concern due to its impact on the human food chain (Ao et al., 2022a; Shahid et al., 2017).

Cr is a redox-sensitive element, and manganese oxides are its main natural oxidant in soil. The transformation from rock-derived chromium (III) to more mobile and hazardous hexavalent Cr (CrO_4^{2-}, $HCrO_4^-$, $Cr_2O_7^{2-}$) has been documented in natural systems like groundwaters (Qin and Wang, 2017). Negatively charged Cr (VI) can be sorbed onto iron oxides or clay minerals, reducing its mobility and risk (Covelo et al., 2008; Dimos et al., 2012; Johnston and Chrysochoou, 2014; Yu et al., 2020a; Zhang et al., 2022). However, Cr (VI) interactions with clay minerals are weak and can be easily disrupted through ion exchange (Covelo et al., 2008; Frank et al., 2019; Rosales-Landeros et al., 2013). Soil organic matter, sulfides, and Fe (II) can convert Cr (VI) to Cr (III), which can then bind to iron oxides or co-precipitate. Soil components like oxides, clay minerals, organic matter, collectively influence the geochemical behavior of Cr in soil systems, with oxides, particularly Fe and Mn oxides, playing a

dominant role. The bacterial activity, experimented using soil incubations have shown that weakly crystalline or amorphous Fe oxides can be reduced, leading to the release of associated metals, including Cr (Quantin et al., 2002).

Tropical and subtropical climates, characterized by heavy rainfall and high temperatures, result in extensive soil weathering and leaching, causing the formation of "red soils" with phyllosilicates and iron, aluminum, and manganese accumulated as oxides (Berger and Frei, 2014; He et al., 2004). Iron and Mn oxides continually dissolve and precipitate, forming iron-manganese nodules (FMNs), which act as important scavengers of soil pollutants, including Cr. FMNs were found to influence the oxidation of Cr (III) to Cr (VI) (Hai et al., 2020), and field studies indicated that Fe and Mn oxides promoted the migration and transformation of chromium in basalt-derived soils (Ao et al., 2022b; Sun et al., 2022; Wille et al., 2018; Zhang et al., 2023). In naturally Cr-enriched soils, such as those found in the ultramafic areas in Brazil and New Caledonia, Cr primarily associates with well-crystallized Fe oxides or chromite, indicating the predominance of stable trivalent chromium. However, notable amounts of hexavalent chromium (plant-available, up to 1,000 mg/kg) have been detected. This occurrence may be linked to the oxidation of Cr (III) by Mn oxides (Becquer et al., 2003; Fandeur et al., 2009; Garnier et al., 2013, 2006), influenced by the use of fertilizers, as Cr (VI) can exchange with phosphates (Becquer et al., 2003), or associated with microbial weathering (Quantin et al., 2002). In floodplain soil profiles, prolonged flooding increases chromium mobility, while chromium solubility is higher below the water table, highlighting the role of soil hydrology in chromium dissolution and migration (Shaheen and Rinklebe, 2014). A gap remains between controlled lab experiments and field studies with more variables impacting chromium dynamics.

Non-traditional isotope techniques have emerged to understand metals and metalloid cycles in modern or paleoenvironments. In red soils, significant isotope fractionation, like that of Cd and Mg isotopes, reveals formation processes linked to FMNs, originating from soil water or granite weathering (Gao et al., 2021, 2018). Redox activity dictates Cr mobility, highlighting the chromium isotope system as a valuable proxy for understanding red soil formation and Cr fate. Recent findings emphasize that redox reactions, particularly the reduction of hexavalent chromium to trivalent chromium, are primary contributors to chromium isotope variability in surface environments (Qin and

Wang, 2017; Wang et al., 2021). Studies have evaluated the effect of single or multiple environmental components on chromium redox and isotopic fractionation. Biotic or abiotic reduction of Cr (VI) to Cr (III) results in enrichment in light isotopes of Cr (III) ($\Delta^{53}Cr = \delta^{53}Cr_{product} - \delta^{53}Cr_{reactant}$, varying between -7.6‰ and -0.4‰), whereas oxidation of Cr (III) results in a variable $\Delta^{53}Cr$ (from -2.5‰ to +1‰) (Qin and Wang, 2017). However, the understanding of isotopic fractionation during Cr (III) oxidation is hampered by limited experimental investigations and an incomplete understanding of the underlying mechanisms.

Cr isotope records in current soil profiles are limited compared to extensive research on ancient paleosols indicating atmospheric oxygenation (Babechuk et al., 2019; Colwyn et al., 2019; Mänd et al., 2022). Berger and Frei (2014) have characterized Cr behavior in Malagasy Madagascar's laterite soil, revealing increased Cr concentration in the uppermost portions of the soil profile, accompanied by a decrease in $\delta^{53}Cr$ values, which is interpreted by a partial immobilization (e.g., by adsorption or co-precipitation of Fe oxides) occurring during the upward migration of mobile Cr (III) from deeper parts of the weathering profile. Co-variation of chromium isotopes with silicon isotopes and iron content, along with significant chromium enrichment and silicon loss found in laterite profile by Wille et al. (2018), underscores the impact of Fe oxides on chromium mobility. In laterite profiles, different $\delta^{53}Cr$ value distribution is linked to parent rock stratification and groundwater levels fluctuations (Paulukat et al., 2015). The migration of weathering fluids in porous layered rocks can lead to uneven chromium loss and fractionation. Additionally, changes in groundwater levels introduce heterogeneity in the Cr isotopic composition and soil organic matter may contributed to chromium fractionation through its ability to reduce isotopically heavy Cr (VI) to Cr (III).

Our study investigates chromium distribution in soil profiles from South China, focusing on paddy and non-paddy soils. These regions are paramount to China's food security strategy, especially in rice cultivation. However, persistent food security challenges have emerged in recent years due to toxic metal contaminants in rice (Huang et al., 2019; Ren et al., 2022). These challenges stem from two primary sources: the naturally elevated geological background, as reported in the karst region of Guangxi (Yang et al., 2021), and anthropogenic activities, notably observed in Hunan Province (Wang et al., 2016). Our research aims to utilize a combination of chemical extraction and chromium stable

isotope techniques to understand differences in Cr partitioning between FMNs and surrounding soils. We seek to identify potential chromium sources and explore key factors influencing chromium cycling in red soil systems with abundant FMNs, thereby enhancing our understanding of chromium behavior. This study provides a scientific basis for assessing soil chromium pollution and food safety in the region. Additionally, it offers insights into the applicability of chromium isotope techniques in natural soil systems.

2. Material and methods

2.1 Study area and sampling

The study was carried out in Wangling Town (109°01′07″E, 23°11′01″N) and Litang Town (109°05′49″E, 23°11′38″N), in Binyang County, Guangxi Zhuang Autonomous Region, in South China. About 8 km separate the two locations. The subtropical monsoon controls the climate here, resulting in an annual precipitation of ~1,491 mm, with a wet season from April to September, accounting for about 78% of the annual precipitation, and a mean annual temperature of 21°C. Carbonated bedrock dominates the region, but red soils are mostly developed from quaternary colluvium deposited over carbonates (Wei et al., 2014). At each site, two soil profiles were sampled: a paddy (rice culture) and a non-paddy soil profile (vegetable culture). The land use has not been modified from at least 40 years. Based on soil texture and color, soil profiles were separated at both sites into several horizons; see details in Table S1. Contrary to the three other profiles, the Litang paddy soil profile is drained at a depth of 40 cm, the outlet water being exported and collected in an artificial cemented reservoir, where rainfall and drained waters are stored and used for irrigation.

For each horizon, approximately 50 kg of bulk soil samples were collected, air-dried, and separated into two parts in the laboratory: FMNs (> 1 mm) and surrounding soil (< 1 mm). The separated FMNs were washed gently with Milli-Q water, dried, and then sieved into three size classes: 1-2 mm, 2-5 mm, and > 5 mm. The nodule proportions of each horizon were determined by weighing each FMN class. Finally, 5-10 g of each sub-sample (FMNs and surrounding soil) were ground in an agate mortar, passed through 0.15 mm sieves, and stored in sealed bags for further analysis. Additionally, to constrain natural and anthropogenic inputs in soils, three samples of bare calcareous

rocks, and seven samples of fertilizers used by local farmers, as well as two samples of irrigation water at the sampling sites of both locations were collected (Table 2). Rocks and fertilizers were ground, dissolved. Water samples (~12 L) were filtered *in situ* through 0.22 μm polyethersulfone membranes (Jinteng, China) and acidified with distilled 16 M HNO_3.

2.2 Physico-chemical properties of soils

All chemicals used in this study were at least analytic grade from Merck company and acids were double-distilled for enhanced purity. Soil properties were determined using bulk soil except for XRD analysis. Soil pH was measured potentiometrically in a soil/water (1:2.5) mixture with a PHS-3C pH meter (Leici, China) (Thomas, 2018). The cation exchange capacity (CEC) was determined by the ammonium acetate saturation technique combined with the titration method (Gillman et al., 1983). Wet sieving in conjunction with the hydrometer technique was used to determine soil texture (Gee and Bauder, 2018). Soil bulk density was estimated by weighing and calculating the dry weight of soil per volume unit (Grossman and Reinsch, 2018). Soil organic matter (SOM) content was evaluated using an oil bath-$K_2Cr_2O_7$ titration method (Nelson and Sommers, 2015). The mineralogical composition of FMNs and surrounding soil (< 0.15 mm fraction) was measured by X-ray diffraction (XRD) analysis using a PANalytical diffractometer with Ni-filtered Cu Kα radiation (at 45 kV and 40 mA) scanning from 5° to 75° 2θ with a scan step of 0.01° at RX platform of Université Paris Cité. The minerals were then identified using X'Pert HighScore Plus software (PANalytical, Almelo, The Netherlands) and quantified using the MAUD program (Material Analysis Using Diffraction) based mainly on the Rietveld refinement method (Lutterotti et al., 1999). Element content was measured by inductively coupled plasma mass spectrometry (ICP-QMS 7900, Agilent) at PARI Analytical Platform of IPGP-Université Paris Cité (hereafter referred to as PARI-IPGP) after HCl-HF-HNO_3 digestion. The USGS geological standards BHVO-2, BCR-2, and Nod-P-1 were used for quality control of sample digestion and elemental analysis. In most cases, the measurement deviation does not exceed 10% of the reference value, and the standard deviation is below 5%.

2.3 Fe oxide extraction using the citrate-bicarbonate-dithionite (CBD) method

Fe oxides were extracted to examine their impact on Cr isotope signatures due to the affinity of Cr towards Fe oxides. A modification of the citrate-bicarbonate-dithionite (CBD) deferrification method from Holmgren (1967) was used to quantify Cr associated with Fe-oxides. One hundred mg of sample was mixed with 40 mL of 0.3 M sodium citrate, 5 mL of 1 M sodium bicarbonate, and 1 g of sodium dithionite, then heated at 80□ for 4 h with manual shaking every 30 min. After centrifugation, the supernatant was removed while the solid residue was kept. The extraction was repeated 3-10 times to ensure that all Fe oxides had been removed. Finally, the residue was rinsed several times with Mill-Q water and dried at 40□ before being weighed, grounded, and stored before elemental and isotope analyses.

2.4 Cr purification and isotope analysis

The chromium purification was achieved by a 2-step column chemistry with cation exchange resin (AG®50W-X8, 200-400 mesh, Bio-Rad) using the procedure modified from Larsen et al. (2016) in a Class 1000 cleanroom (PARI-IPGP). Since Cr isotope fractionation can occur during the chemical separation through chromatographic columns and the final purification yields rarely exceed 70-80%, we used a double spike technique following the protocol detailed in Sossi et al. (2018).

First, samples containing 1 µg Cr were spiked with an appropriate ^{50}Cr-^{54}Cr double spike solution volume to achieve a Cr_{spike}/Cr_{sample} ratio of ~0.28. The spiked samples were heated in 6 M HCl at 100□ for 24 h to facilitate homogenization and promote the formation of Cr-Cl complexes. Then, cold Milli-Q water (4□) was added to dilute the HCl concentration to 1 M. Sample was loaded into a pre-cleaned and conditioned column of 1 mL resin, and Cr was collected immediately. Further elution of Cr was carried out in 5 mL of 1 M HCl, and both eluates were evaporated together. The resin was washed with 10 mL of 6 M HCl and 5 mL of Mill-Q water. After that, the Cr fractions were exposed to 0.5 M HNO_3 and 0.8% H_2O_2 at room temperature for at least 48 h to facilitate the conversion of all Cr species to Cr^{3+}. The remaining major elements (e.g., Al) as well as interferents (Ti, V, and Fe) were removed by loading the sample onto the pre-conditioned AG®50W-X8 resin followed by elution with 5 mL of 0.5 M HF and 22 mL of 1 M HCl. Finally, Cr was eluted with 10 mL of 2 M HCl, evaporated, and the Cr concentration was adjusted to ~100 µg/L with 2% HNO_3 for isotope measurement.

188 The Cr isotope compositions were measured on a Neptune Plus MC-ICP-MS (ThermoScientific)
189 equipped with a PFA μFlow nebulizer (100 μL/min), an Apex HF desolvation introduction system
190 (Elemental Scientific) and eight Faraday collectors that allowed for simultaneous collection of ^{50}Cr,
191 ^{52}Cr, ^{53}Cr, ^{54}Cr together with ^{49}Ti, ^{51}V and ^{56}Fe, to correct the isobaric interferences of ^{50}Ti, ^{50}V, and
192 ^{54}Fe on ^{50}Cr and ^{54}Cr, respectively. In the medium resolution mode, a 4-8 V sensitivity on ^{52}Cr was
193 obtained for a 100 μg/L Cr solution using Jet sample and H skimmer cones. The purification yield of
194 our method (~80%) is in line with previous studies (Zhu et al., 2018, 2019). The procedural blanks of
195 0.2-11 ng (n = 7), are negligible compared to the loaded sample mass (1000 ng). Isotope results are
196 reported as δ^{53}Cr and normalized to the certified Cr isotopic standard NIST SRM 979 as Eq. (1):

197 $$\delta^{53}Cr(‰) = \left(\frac{(^{53}Cr/^{52}Cr)_{sample}}{(^{53}Cr/^{52}Cr)_{NIST\ SRM\ 979}} - 1\right) \times 1000 \quad (1)$$

198 Reproducibility and accuracy of isotope measurements were checked using the NIST SRM 3112a
199 and USGS BHVO-2 reference materials, resulting in δ^{53}Cr of -0.09 ± 0.03‰ (2SD, n = 9) and -0.14 ±
200 0.05‰ (2SD, n = 27), respectively, which agreed with reported values in the literature (Liu et al., 2019;
201 Wu et al., 2020).

202 **3. Results**

203 3.1 Soil physicochemical properties

204 The key physicochemical properties of the soils are listed in Table 1. Neutral pH values (7.2 ±
205 0.13) are found in most soil horizons except for the non-paddy soil profile in Wangling (pH ~4.8) and
206 the topsoil horizon of the two paddy soil profiles in Wangling (pH 6.2) and Litang site (pH 6.5). The
207 difference in soil pH may be attributed the different crops and the recycling of organic material, which
208 tends to acidify soil (Butterly et al., 2013; Wei et al., 2006). The SOM content is higher in the surface
209 horizon and decreases with depth. Overall, paddy soils have more SOM than non-paddy soils because
210 a small portion of above-ground rice stalks and underground roots remains in the field after rice harvest,
211 where intermittent reducing conditions promote their decomposition. The soil density ranges from 0.9
212 to 2.3 g/cm^3, with the minimum and maximum values observed in the Litang paddy soil profile.
213 Additionally, there is a gradual increase in soil density with depth within this profile, finally reaching
214 approximately twice the value of the bottom horizon in the Wangling paddy soil profile. Soil CEC and

clay content increase with depth, ranging from 11.8 to 24.1 cmol/kg and 16 to 40%, respectively.

3.2 Distribution and mineralogy of FMNs and surrounding soils

In all soil profiles, except with of the Litang paddy soil profile, FMNs content in each size class and across each soil profile exhibits relatively low variability (Table 1). In particular, both non-paddy soil profiles have a dominant FMNs content (61-76% of the total) over the surrounding soil, while the paddy soil profile at Wangling has a lower FMNs content (37-51%). On the other hand, the Litang paddy soil profile shows a gradually increase in the total FMNs content with depth, ranging from ~5% in the top to 45% in the bottom horizon. This increase affects each FMNs size class. In soil profiles, most FMNs are found in the 2-5 mm class (~66%), followed by the > 5 mm class (~23%), and the 1-2 mm class (~10%).

Mineral compositions of FMNs are generally similar independently of size or soil horizon (Fig. S1, Table S2); we now discuss these FMNs as a whole compared with the surrounding soils, as depicted in Fig. 1. In both non-paddy and paddy soil profiles of Wangling, the mineralogy remains constant with depth irrespective of fraction (surrounding soils and FMNs, Figs. 1a and 1c, Table S2). Specifically, the surrounding soil at Wangling is primarily composed of ca. 35-40% kaolinite, 30-35% quartz, 10-15% gibbsite, and 10-15% goethite, whereas the FMNs encompass 60-65% goethite, 15-20% gibbsite, and 10-15% kaolinite. However, distinctions in mineralogical composition are noticeable between non-paddy and paddy soil profiles in Litang. In the Litang non-paddy soil profile, from top to bottom, the surrounding soil is affected by a decrease in quartz (55 to 35 %) and microcline (10 % to traces) and a rise in kaolinite (35 to 65%) proportions (Fig. 1b). A similar vertical evolution of the quartz-kaolinite couple is also observed in the surrounding soil of Litang paddy soil profile (Fig. 1d). The 15 % of illite found in the upper horizons are progressively replaced by microcline at intermediate depth. The deepest sample is almost exclusively composed of kaolinite and quartz. FMNs in both profiles are primarily constituted of 60-80 % iron oxides (mostly goethite) and 10% quartz (Fig.1b and 1d). Kaolinite represents 10-30 % of the nodules, except in the waterlogged horizon (Brg, 45-70 cm) in the Litang paddy soil profile where it is almost absent. Mn-rich phases (e.g., birnessite) have not been observed in either FMNs or surrounding soil samples, primarily due to their low

abundance or to the presence of Mn as impurities in other minerals like iron oxides (Wang et al., 2023).

3.3 Vertical distribution of elements in soil profiles

The concentrations of Cr and other key elements are listed in Table S3 and plotted in Fig. S2. High Mn concentrations (up to 24 g/kg) are only found in the largest FMNs of two horizons of the non-paddy Litang profiles, showing that overall FMNs should be better defined as iron nodules only. Compared to the surrounding soils, FMNs contain higher redox-sensitive trace elements such as V, Cr, and Fe. Conversely, higher concentrations of immobile elements (e.g., Ti) or major and soluble elements (e.g., Mg) are reported in the surrounding soils. In the surrounding soils, Cr concentrations are higher in Wangling (223-247 μg/g) than those in Litang (95-180 μg/g) and relatively independent of the cultivation mode (paddy vs. non-paddy). Across all soil profiles, Cr content is higher in the smallest FMNs (822-1,451 μg/g) than in the largest ones (325-693 μg/g).

To evaluate the potential accumulation or depletion of elements throughout the soil profile, the mass balance coefficient (τ) was applied (Braun et al., 1993) according to Eq. (2):

$$\tau_{X,Nb} = \frac{(C_X/C_{Nb})_{sample}}{(C_X/C_{Nb})_{parent}} - 1 \quad (2)$$

where C_X and C_{Nb} are the concentrations of element X and niobium in soil samples or parent materials, respectively. The corresponding values in the deep Quaternary red earth reported by Yang (2006) were used as those in the parent materials, since our soil profiles were developed from quaternary colluvium. Niobium was selected as an immobile element due to its stability during advanced weathering processes (Guinoiseau et al., 2021). As indicated in Fig. 2, the τ values of immobile elements (Al and Ti) remain constant across all soil profiles, suggesting a similar conservative behavior of Nb. The major and soluble element (Mg) shows a slight depletion. The reactive element (Mn) behavior is comparable to that of Mg in the Wangling soil profiles. In contrast, in Litang soil profiles, Mn displays either pronounced depletion (in the paddy soil profile) or enrichment (in the non-paddy soil profile). The redox-active elements (Cr, V, Fe) show strong enrichment, particularly in the non-paddy soil profiles. Significant enrichment of redox-active elements is observed mainly in the Brg horizon (45-70 cm) downwards in the paddy soil profile of Litang, which contrasts with the trend observed in Wangling.

To assess the extent of soil weathered erosion throughout the soil profile, we applied the soil-weathered erosion coefficient (ba), using the content of the following oxides, as described by Zhang et al. (2004):

$$ba = \frac{(Na_2O+MgO+K_2O+CaO)}{Al_2O_3} \quad (3)$$

This coefficient indicates the degree of leaching of soil base ions. Al_2O_3 is more stable and less susceptible to washing away during soil formation than Na_2O, MgO, K_2O, and CaO. Thus, the greater the leaching effect of soil weathering, the lower the ba value. As shown in Table 1, the ba values are generally low (≤ 0.07), except in the Litang paddy profile where ba values are notably higher, peaking at 0.19 at the surface but gradually decreasing with depth to 0.09 at the bottom. This indicates that the Litang paddy profile experiences weaker and more variable soil-weathered leaching compared to the other profiles.

3.4 Effect of Fe oxides on element partitioning via CBD extraction

For comparison, the CBD extraction was conducted on the two soil profiles from Litang, to determine: 1) the main carrier of Cr both in FMNs and surrounding soils, 2) the respective Cr isotope signatures of the oxides (FeO hereafter, extracted fraction) and silicate phases (ReS hereafter, residual fraction), and 3) whether the observed $\delta^{53}Cr$ values shape in the Litang paddy soil profile is associated with Fe oxide or silicate phases. The paddy soil profile has a heterogeneous elemental distribution (Table S3 and Fig. S2) and the lowest and the most variable FMNs content (Table 1) with depth. In contrast, the non-paddy soil profile is characterized by a homogeneous elemental distribution and a higher and more stable FMNs content with depth. In addition to the surrounding soil fraction, the medium-sized FMNs (2-5 mm) were also included since this fraction represents 58-71% of the total FMNs mass in these profiles. The results are reported in Fig. 3 and Table S4. Specifically, the ReS fraction of the surrounding soil and FMNs has similar low Cr concentrations (60-130 mg/kg, Fig. 3a) in non-paddy and paddy soils. The FeO fraction of the FMNs contains the highest Cr concentrations (800-1000 mg/kg), while Cr concentrations in the FeO fraction of the surrounding soil are intermediate (200-400 mg/kg). Additionally, in the 2-5 mm FMNs, the CBD extraction removed almost all Fe, Mn, and Cr (> 90%), indicating that Cr is almost entirely carried by Fe and Mn oxides in FMNs. In the

surrounding soils, however, the extraction yield of Cr (50-75%) is lower than for Fe and Mn (80-95%), demonstrating that Cr is carried by oxides and silicates (illite, kaolinite or microcline, cf. Fig. 1). Further, although the Fe extraction yield is almost constant in the Litang paddy soil profile (80-85%), the Cr and Mn extraction yields appear to be at their maximum in the waterlogged horizon (Brg, 45-70 cm). This may imply that the waterlogged conditions in this horizon strongly influences the behavior of Cr and Mn.

3.5 Cr isotope signature in soil profiles

Chromium isotope signatures of FMNs and soil samples are reported in Fig. 4 and Table S3. Heavier Cr isotope signatures are observed in FMNs compared with the surrounding soils (Figs. 4a, 4b, 4d and 4e). Between the different FMNs size classes, Cr isotope signature does not vary much, with a mean value of 0.78 ± 0.17‰ (n = 45), which is not correlated with the enrichment of Cr in the smallest FMNs (Table S3 and Fig. S2). Regarding the surrounding soils, δ^{53}Cr values are constant and cluster around 0.32 ± 0.07‰ across all soil profiles except for the Litang paddy soil profile. Conversely, the surrounding soils of Litang paddy soil profile demonstrate a clear increase in δ^{53}Cr values with depth, ranging from 0.02 ± 0.05‰ in the topsoil to a maximum of 0.38 ± 0.06‰ in the waterlogged horizon (Brg horizon, 45-70 cm), and decreasing to 0.19 ± 0.03‰ in the bottom horizon (Fig. 4e and Table S3).

The chromium isotope signatures of the two fractions isolated by CBD extraction differ significantly (Table S4 and Figs. 4c, 4f). Because of the high Na concentration in the FeO extract, the analysis of chromium isotope signatures associated with iron oxides cannot be performed directly. Therefore, to determine the $\delta^{53}Cr_{FeO}$, we calculated the extracted mass of iron oxides ($Mass_{FeO}$) and its element content (X_{FeO}), assuming that Nb is resistant to CBD extraction and is concentrated in the residue:

$$Nb_{ReS} \times (Mass_{total} - Mass_{FeO}) = Nb_{total} \times Mass_{total} \quad (4)$$

then the extracted ratio and X_{FeO} were calculated according to:

$$Mass_{FeO}/Mass_{total} = 1 - Nb_{total}/Nb_{ReS} \quad (5)$$

$$X_{FeO} = (X_{total} - X_{ReS}) \times Mass_{total}/Mass_{FeO} + X_{ReS} \quad (6)$$

and by combining the known Cr concentration and isotope composition in the total material and in the ReS fraction, we determined the $\delta^{53}Cr_{FeO}$ according to Eq. (7):

$$\delta^{53}Cr_{FeO} = \frac{(Nb_{ReS} \times Cr_{total} \times \delta^{53}Cr_{total} - Nb_{total} \times Cr_{ReS} \times \delta^{53}Cr_{ReS})}{(Nb_{ReS} \times Cr_{total} - Cr_{ReS} \times Nb_{total})} \quad (7)$$

As shown in Fig. 4c, in the non-paddy soil profile of Litang, the $\delta^{53}Cr$ values are not only constant with depth but also quite similar for ReS (mean: 0.23 ± 0.06‰), for FeO fractions (mean: 0.33 ± 0.11‰) of the surrounding soils and for ReS fraction extracted from the FMNs (mean: 0.36 ± 0.10‰). However, the FeO fraction of the FMNs has a higher $\delta^{53}Cr$ signature (0.76 ± 0.10‰), showing a likely isotope fractionation before or during Cr incorporation within Fe oxides. Litang paddy soil profile, however, presents a quite different picture (Fig. 4f). In this profile, the $\delta^{53}Cr$ values for the FeO fraction are always heavier than the ReS fraction in the FMNs and the surrounding soil, and the $\delta^{53}Cr$ values for the ReS fraction in FMNs and surrounding soils are stable with depth but with a heavier signature in the former ($\Delta^{53}Cr_{ReS\_FMN\text{-}ReS\_Soil}$ of 0.53‰). While the gap between FeO and ReS' $\delta^{53}Cr$ is constant within the FMNs and close to the one measured in the Litang non-paddy soil profile ($\Delta^{53}Cr_{FeO\text{-}ReS}$ of 0.35 ± 0.18‰), significant variations are noticed within the surrounding soil. A maximum value of $\Delta^{53}Cr_{FeO\text{-}ReS}$ is being observed in the waterlogged horizon (Brg, 45-70 cm), suggesting that Cr redistribution through redox processes and/or its coprecipitation within Fe oxides or FMNs may be the main drivers of the observed $\delta^{53}Cr$ changes.

3.6 Water, rock and fertilizer samples

The chromium isotope compositions and the element contents of these samples are listed in Table 2. Irrigation waters from Wangling and Litang have low chromium contents of 0.07 and 0.28 μg/L, respectively. Calcareous rocks exhibit high calcium contents of up to 40% (consistent with their mineral composition of > 90% dolomite or calcite) and chromium contents of 4 mg/kg. The N-P-K compound fertilizers typically contain 10-20% phosphorus and potassium, with potassium primarily being in the form of potassium chloride, except for F3. The chromium content of the fertilizer ranges from 16 to 26 mg/kg. At the same time F3 where potassium is predominantly in the form of potassium sulfate derived from the dichlorination of potassium chloride, has a lower chromium content of 9 mg/kg, likely due to chromium loss during dechlorination.

Wangling and Litang irrigation waters have very different $\delta^{53}Cr$ values, 1.47 ± 0.06‰ and 0.16 ± 0.02‰, respectively (Table 2). The irrigation water in Wangling originates from a natural stream, and therefore its $\delta^{53}Cr$ value and Cr/Ca ratio are similar to those of calcareous rocks. In contrast, the irrigation water in Litang is stored in an artificial cemented reservoir, which primarily serves to collect rainwater during rainfall events and functions as a drainage pond for paddy fields. Consequently, its $\delta^{53}Cr$ value is similar to the surrounding soils in paddy fields. Calcareous rock samples have generally high $\delta^{53}Cr$ values (mean 1.01 ± 0.58‰, n = 3), while fertilizer samples have $\delta^{53}Cr$ values ranging from 0.1‰ to 0.5‰, except for F3 (1.49 ± 0.12‰). The high $\delta^{53}Cr$ value of F3 can be attributed to the preferential loss of light chromium isotopes during its dechlorination.

4. Discussion

4.1 Origin of chromium in red soils: a source effect?

Soil profiles have consistent chromium isotopic signatures for FMNs and most of surrounding soils, except for the Litang paddy soil profile, which shows variability. To identify if a source effect can explain the variations observed in these red soils, we need to assess input and output fluxes and compare them to the average Cr concentrations.

As a first step, the average Cr concentration and soil density of soil profiles can be used to calculate soil Cr stocks in the cultivated soil horizon in 0.3 m^3 box (Fig. 5) according to Eq. (8):

$$Soil\ Cr\ stock\ (g) = Soil\ density\ (g/cm^3) \times Cr\ (mg/kg) \quad (8)$$

Comparing Cr stock, external inputs (fertilizer, rainfall, and irrigation water) and outputs (harvesting, drainage), per unit area reveals significant differences. As shown in Fig. 5, Wangling non-paddy and paddy soil profiles hold 259 g/0.3 m^3 and 176 g/0.3 m^3 of Cr, while Litang has 220 g/0.3 m^3 and 43 g/0.3 m^3, respectively. Before to analyse Cr cycle in a whole, we assess the "active" Cr stock, i.e. reactive to current pedological conditions by evaluating in details the mineralogical composition and the primary Cr carriers. In red soils, surrounding soils must be decoupled from FMNs story. Indeed, a significant difference has been measured for the residual $\delta^{53}Cr$ signature after CBD extraction in the surrounding soil ($\delta^{53}Cr$ = -0.02 ± 0.10 ‰) and the FMNs (0.51 ± 0.09 ‰) of the Litang paddy soil profile (Fig. 4f), despite a similar mineralogy (abundant kaolinite and quartz, Fig. 1d) and Cr

concentrations (Fig. 3a).

The most plausible explanation is that these two components, surrounding soils and FMNs, are at different formation stages, with FMNs serving as ancient archives that persist. This aligns with findings in the literature, where evidences like old ^{14}C formation ages for FMNs (Pai et al., 2003) and insights from 3-D microstructure analysis (Yu et al., 2020b) support this view. Therefore, FMNs should be seen as historical and chemically stable archives unaffected by current pedological conditions, rather than as recent and reactive mineral phases. In surrounding soils, Cr can be associated with primary minerals like illite/microcline or secondary products such as kaolinite and gibbsite in Wangling. Despite no iron oxides has been detected by XRD analysis, amorphous phases like ferrihydrite can constitute a notable portion (10-30 wt%) based on Fe concentrations in bulk samples (3.8-9.4 wt%, Table S3) and the effectiveness of Fe removal by CBD extraction reported for Litang profiles (80-95%, Fig. 3b). The high percentage (50-75 wt%) of chromium removed by CBD extraction in surrounding soils suggests that these amorphous iron oxides are a major carrier of Cr in this fraction (200-400 μgCr/g, Fig. 3a and Table S4). The Cr concentration in the ReS fraction (60-80 μgCr/g) and the prevalence of quartz and kaolinite indicate the latter as a significant Cr-carrying phase in red soils. A simple mass balance gives a 120-350 μgCr/g kaolinite, larger than the UCC value (92 μg/g, Rudnick and Gao (2014)), but in line with the immobile behaviour of Cr during chemical weathering. Thus, if the surrounding soil is considered as the Cr source available for chemical weathering (formation of kaolinite/gibbsite) or oxidative dissolution (iron oxide precipitation), this "active" Cr stock amounts to 22 and 32 g/0.3 m^3 in the Litang non-paddy and paddy soil profiles, respectively (Fig. 5).

Regarding the input, atmospheric deposition, including rainwater and dust, can be a significant source of soil metal contamination (Fu et al., 2021). Rainwater in the area has low Cr levels (≤ 1 ppb) and with an annual rainfall of ~1,491 mm (Gao et al., 2021), the maximum rainwater Cr flux of 1.5 mg/m^2/yr (F_{rain}, Fig. 5). Human-made dust deposition is negligible due to the absence of factories. Natural dust deposition, following Kok et al. (2021), ranges from 1 to 3 g/m^2/yr, giving a Cr flux of 0.09 to 0.28 mg/m^2/yr (F_{dust}, Fig. 5), about ten times lower than rainwater input.

Irrigation water, as a Cr source in soil, differs between Wangling and Litang. In Wangling, river-based irrigation with low Cr content (0.07 μg/L) yields a Cr flux (F_{irw}, Fig. 5) of 0.1 mg/m^2/yr. In

Litang, water reservoirs receive rainwater and drained water, resulting in a higher Cr concentration (0.28 µg/L) due to soil interactions, leading to a Cr flux of 0.2 mg/m^2/yr for non-paddy fields. However, for the Litang paddy soil profile, this water cannot be considered an external input as most of the Cr originates from drainage within the soil.

Fertilizers impact soil Cr levels. We analyzed seven local fertilizers (Table 2) used for rice and vegetable cultivation. On average, 1,500 kg/ha/yr of fertilizer is applied in paddy fields, and 1,500-3,000 kg/ha/yr in non-paddy fields. With fertilizers containing 20 mg/kg Cr, estimated Cr flux is 3-6 mg/m^2/yr (F_{fer}, Fig. 5). Notably, widespread fertilizer uses in China began after 1980. Over 40 years, it contributes about 0.12-0.24 gCr/m^2, less than 1.1% of the soil's "active" Cr stock. Fertilizers are not the primary Cr source in the soil.

Cr outputs from soil profiles are limited to crop uptake and runoff. Crop uptake comprises vegetables and rice for non-paddy and paddy soil profiles. In Guangxi Zhuang Autonomous Region, vegetable yield averages 2.2 kg/m^2/yr (Ministry of Agriculture, 2016), with a Cr concentration of 0.3 mg/kg, resulting in a Cr output of about 0.7 mg/m^2/yr (F_{veg}, Fig. 5). For Cr export through rice harvesting, most of the Cr remains in rice roots after harvest. With a Cr concentration of 0.2 mg/kg in rice grains (Xiao et al., 2018) and an aboveground plant biomass of 1.2 kg/m² for rice (Roy et al., 2012), the estimated Cr export from rice cultivation is approximately 0.5 mg/m^2/yr (F_{rice}, Fig. 5).

Estimating Cr runoff is challenging. In Litang, due to the absence of major water bodies, it is likely negligible. In Wangling, the river draining the fields shows low Cr levels and isotope features aligned with calcareous formations within the basin, suggesting a negligible Cr flux outside the field area.

Input and output fluxes are depicted in Fig. 5. Fertilizers' impact over 40 years is negligible at the soil formation scale. The net Cr enrichment in soils ranges from 1.0 to 1.4 mg/m^2/yr based on long-term inputs and outputs. This rate would require 15,700 to 32,000 years to build the "reactive" Cr pool in surrounding soils, inconsistent with its recent nature. Hence, the primary Cr source in soils is likely the chemical weathering of colluvium parent minerals, influenced by changes in redox conditions.

4.2 Land use or hydrological control on elemental distribution in soils

Distinct land use may play on soil hydrology, which could influence Cr mobility or distribution within paddy and non-paddy soils. Mineralogically, all soil profiles comprise FMNs rich in goethite (60-85%, Fig. 1) and some accessory minerals (quartz, kaolinite, and gibbsite). The FMNs are more abundant in non-paddy soil profiles than in paddy ones, and only the Litang paddy soil profile shows a variability of FMNs content with an increase in depth. The surrounding soils are mostly an assemblage of quartz and kaolinite, but gibbsite and iron oxides can be found at Wangling sites (Figs. 1 and S1). At Litang, illite or microcline are found in the top horizons, while amorphous iron oxides, not detected by XRD analysis, can reach 10-30 % (see section 4.1). In modern soils, illite is frequently found under moderate weathering intensity compared with gibbsite and kaolinite, typical of intense chemical weathering, such as faced red soils (Churchman et al., 2012). Gibbsite typically occurs in soils with insufficient Si supplies under intense leaching, while kaolinite forms in soils with weak leaching and high Si availability (Berger and Frei, 2014; Churchman et al., 2012). Our data suggest that soils in Wangling are facing more extreme chemical weathering than in Litang, as confirmed by the lower ba values observed in Wangling. Therefore, the location (Wangling vs. Litang) rather than the land use (vegetable vs. rice culture) seems to dictate the soil hydrology that will condition the mineralogy and the distribution of elements throughout the soil profile. The lower elevation at Wangling (94 m, Table S1) than at Litang (101 m) may result in a shallower groundwater level, subjecting the entire soil profile to long-term fluctuations in groundwater and consequently enhancing soil leaching intensity. In contrast, in Litang, prominent gleying features are observed within the Brg horizon (45-70 cm) of the paddy soil profile, resulting from localized waterlogging. The soil density can be a controlling factor here since its values at the bottom of the Litang paddy soil profile are approximately twice that of Wangling. Consequently, the compactness of the soil at the bottom of the Litang paddy soil profile acts as a barrier, restricting or slowing down the downward movement of water. This restricted permeability contrasts to the porous and permeable nature of the loose soil in the bottom horizon of the Wangling paddy soil profile. Another controlling factor may be the water drainage at 40 cm in the Litang paddy soil profile. Adjacent to this profile lies a cemented water reservoir, and a drainage pipe is connected to the Litang soil profile, positioned approximately 40 cm below the ground, to collect drainage from it. As a result, the upper 40 cm of this profile, including the

460 Ap1, Ap2, and AB horizons, remain consistently dry during periods of non-rice cultivation, in stark
461 contrast to the horizons below, which exhibit gleying features. Therefore, hydrological conditions are
462 a key driver shaping the red soil profiles. By noticing the distinct behaviour of the Litang paddy soil
463 profile, it is also clear that local change in hydrological conditions influences the soil redox conditions
464 and thus plays on the distribution of redox-sensitive elements such as Cr. The principal component
465 analysis (PCA, Fig. S3) based on element concentrations of soil profiles confirms that redox-sensitive
466 elements (Fe, Cr, As, and V) behave similarly, as already observed in other studies (Aide, 2005; Ettler
467 et al., 2017), and consistent with a redox control. Based on the reactivity of Cr isotopes to redox
468 changes (e.g., Wei et al. (2020), such a redox control should be seen in our soil Cr isotope signatures.

469 4.3 Highlighting the effect of redox cycling on Cr mobility using Cr isotopes (Litang soils)

470 The link between redox conditions and Cr isotope variations has been reported in numerous
471 studies on paleosols and laterites (i.e., red soils). A typical negative δ^{53}Cr values is due to the loss of
472 Cr though oxidative weathering (Berger and Frei, 2014; Crowe et al., 2013). This is attributed to the
473 preferential oxidation of the heavy isotopes of Cr during the conversion of Cr (III)-bearing minerals to
474 more soluble and mobile Cr (VI), leading to residual materials enriched in light isotopes. Meanwhile,
475 the positively fractionated mobile pool of Cr (VI) may be transported via runoff to water bodies, as
476 supported by the isotopically heavier δ^{53}Cr values of rivers and oceans (D'Arcy et al., 2016; Sun et al.,
477 2019). However, positive δ^{53}Cr values and Cr enrichment have also been observed in some weathering
478 profiles, which have been explained as the re-deposition of the isotopically heavy fraction of Cr (VI)
479 (Berger and Frei, 2014; Crowe et al., 2013).

480 Taken as a bulk, our red soil profiles all exhibit more positive δ^{53}Cr values (bulk samples all
481 cluster around 0.7‰, except for the mildly positive values (~0.3‰) in the upper part of the Litang
482 paddy soil profile, Fig. 4) than the δ^{53}Cr reported for soils from different geobackgrounds (as
483 summarized in Table S5). Remarkably, all FMNs have a constant enrichment in Cr, Fe, and Mn as well
484 as a similar heavy δ^{53}Cr signature, but clear correlations between δ^{53}Cr values and the inverse of Cr or
485 Fe concentration exist (*Pearson coefficients r* = -0.91 and -0.93, respectively), and are mostly driven
486 by the soil samples from the Litang paddy soil profile (Fig. 6). A robust correlation between Cr and Fe

enrichments has been identified in other weathered soil profiles, where Fe oxides (e.g. goethite, hematite) serve as the primary Cr-bearing minerals, exerting control over the mobility and redistribution of chromium (Becquer et al., 2003; Garnier et al., 2013, 2006; Sun et al., 2022). The weaker correlation between $\delta^{53}Cr$ values and the inverse of Mn concentration (*Pearson coefficients r* = -0.74, Fig. S4) can be attributed to the fact that Mn is likely driving the release of Cr, from minerals through the oxidation, inducing a decoupling of Cr and Mn concentrations. Reversely, Fe serves as a key driver for the sequestration of Cr, effectively immobilizing the released Cr within Fe oxides. This statement is validated by the CBD extraction performed on both surrounding soils and FMNs of the Litang soil profiles, where the Cr concentration in the FeO fraction is much higher than that in the ReS (Fig. 3a), indicating that the majority of Cr is carried by Fe oxides. It is particularly valid in FMNs, where almost all Cr is bound or within goethite, while in the surrounding soils, Cr is significantly associated to silicate minerals like kaolinite (Figs. 1 and 3b). The isotope signatures of the two Cr pools (ReS and FeO) indicates a systematic enrichment in heavy isotopes in the FeO fraction for both surrounding soils and FMNs (Figs. 4c and 4f). In the section 4.1, we have concluded that Cr sequestered in Fe oxides is mostly resulting from ancient (in FMNs), or recent (in surrounding soils) parent material weathering. We thus propose that the enrichment in heavy isotopes in iron oxides is directly linked with a pool of heavy Cr (VI) mobilized by oxidative weathering in our red soil profiles, and which is largely coprecipitated, as other researchers have speculated (Berger and Frei, 2014; Crowe et al., 2013). However, the magnitude of the Cr isotope fractionation between FeO and ReS is less variable for FMNs throughout the profile ($\Delta^{53}Cr_{FeO\text{-}ReS}$ of ca. 0.35‰) than for the surrounding soils ($\Delta^{53}Cr_{FeO\text{-}ReS}$ ranging from 0.0 to 0.6‰). Based on the distinct history of FMNs and surrounding soils (see section 4.1), it points towards different scenarios of Cr precipitation within Fe oxide phases.

Firstly, FMNs are initially formed as pore fillings in soils (Yu et al., 2020b), and consist of Fe from the surrounding soil matrix and the Fe oxides newly formed through the oxidation and precipitation of Fe^{2+} in the soil solution revealed by Fe isotopes (Feng et al., 2018; Sipos et al., 2023). As a result, FMNs may encapsulate Cr from the soil matrix and adsorb/co-precipitate Cr from the solution (mainly as Cr (VI) species like CrO_4^{2-}, $HCrO_4^-$, $Cr_2O_7^{2-}$) during Fe oxide formation. Numerous studies have shown that significant amounts of Cr (VI) can be adsorbed and incorporated into the

structure during the formation and transformation of Fe oxides, and the presence of organic matter and Mn (II) can enhance the adsorption (Liang et al., 2021a; Yu et al., 2020a). Adsorption of Cr (VI) by goethite does not cause significant isotope fractionation according to Ellis et al. (2004), thus Cr (VI) is quantitatively sequestered without isotopic fractionation in the FMNs. These findings indicate that the isotopically heavy Cr (VI) from the soil solution is the most likely source of the Fe oxide-associated Cr in these FMNs. This also explains why FMNs of varying sizes have similar Cr isotopic characteristics despite differences in Cr content. We first hypothesized that the larger surface area of smaller FMNs might lead to an increase of chromium absorption compared to larger nodules. However, scanning electron microscopy pictures (unpublished data) revealed an absence of circular or ring-like structures within the FMNs, and the external layers displayed no noticeable chromium enrichment. FMNs probably formed in one step rather than gradually evolving from smaller to larger sizes. This suggests that higher chromium concentrations might have been found in the soil solutions during the genesis of the smaller FMNs, thereby facilitating chromium accumulation. To validate this hypothesis, further experiments such as CBD extraction from FMNs of varying sizes and the application of methodologies like C^{14} are essential. Regarding the FMNs stability with time, Cornu et al. (2009) showed that Fe oxides in FMNs were not dissolved by redox shifts. Additionally, Quantin et al. (2002) demonstrated that well-crystalline Fe oxides resist to bacterial reduction and reducing conditions, while amorphous and poorly crystalline Fe oxides do not. Given that Cr in our FMNs is mostly carried by crystalline Fe oxides (i.e. goethite, Fig. S1), the FMNs may be stable against soil redox oscillation at later stages, thus minimizing the risk of Cr release. However, further dissolution experiments are needed to confirm this hypothesis, as FMNs from different soils or regions display distinct features and may exhibit variations in their dissolution behavior.

Secondly, for the surrounding soils, where iron oxides are amorphous or weakly crystalline, the $\Delta^{53}Cr_{FeO\text{-}ReS}$ is almost null in the non-paddy soil profile while it is variable and maximal in the waterlogged horizon (Brg) in the paddy soil profile. This limited $\Delta^{53}Cr_{FeO\text{-}ReS}$ could potentially be attributed to fractionation caused by preferential uptake of Cr (VI) by surface vegetation. This uptake may occur through phosphate or sulfate carriers due to the structural resemblances they share with Cr (VI) (Ao et al., 2022a), finally leaving behind Cr (III) enriched in lighter isotopes in the soil. However,

543 this hypothesis fails to elucidate the observed variations in $\delta^{53}Cr$ values within non-cultivated horizons,
544 where the penetration of plant roots is restricted. Moreover, as discussed earlier, we have demonstrated
545 that the Cr output flux caused by plant uptake does not have a significant impact on soil Cr stock and,
546 thus, should have a limited influence on the soil chromium isotope signatures.

547 Alternatively, the presence of more soluble Cr (III) species, such as organic-Cr (III) complexes,
548 in the surrounding soils might also contribute to the limited $\Delta^{53}Cr_{FeO\text{-}ReS}$. Previous researches have
549 demonstrated that soil acidity and organic matter facilitate the dissolution of Cr (III)-bearing minerals
550 (Li et al., 2022; Sun et al., 2022).

551 For the Litang paddy soil profile, the limited $\Delta^{53}Cr_{FeO\text{-}ReS}$ of the surrounding soils in the upper
552 part may be attributed to the unique drainage characteristics of this profile, as discussed in the section
553 4.2. This specific drainage system could have led to the removal of a portion of isotopically heavy Cr
554 (VI) from the soil solution in the upper part of the profile through drainage. Consequently, the soil iron
555 oxides in this region are unable to capture this portion of Cr, resulting in lighter $\delta^{53}Cr$ values and lower
556 Cr concentrations (Fig. 3a) compared to the Brg horizon. Furthermore, Bonneville et al. (2009) and
557 Quantin et al. (2002) established that amorphous and weakly crystalline forms of iron oxides exhibit
558 greater solubility compared to their crystalline counterparts. Soil incubation experiments have
559 demonstrated that during anaerobic phases, the reduction of Fe (III) oxides not only releases
560 structurally bound chromium but also induces the breakdown of soil aggregates and the dissolution of
561 organic matter. This process indirectly mobilizes chromium (Zhang et al., 2023). Conversely, in
562 aerobic conditions, the oxidation of Fe (II) to form Fe (III) oxides, followed by subsequent
563 recrystallization, initiates the reaggregation of soil colloids, leading to the incorporation of chromium.
564 Therefore, the variability of $\delta^{53}Cr$ within the FeO fraction of the surrounding soils in this profile may
565 also be directly linked with the dynamics of redox conditions. Based on their lower crystallinity (as
566 evidenced by the absence of iron oxide minerals detected by XRD, Fig. 1) than in FMNs (Cornu et al.,
567 2009), the Fe oxides within the surrounding soils are expected to exhibit higher solubility and reactivity,
568 potentially leading to variations in $\delta^{53}Cr$ values. The highest $\delta^{53}Cr$ value and CBD-extractability of Fe,
569 Mn, and Cr measured in the waterlogged horizon (Brg, 45-70 cm) imply repetitive cycles of iron oxide
570 dissolution, Cr oxidation by Mn oxides and subsequent sequestration on Fe oxides, resulting in

571 elevated $\delta^{53}Cr$ values. Indeed, it has become clear that Cr (III) oxidation is constrained by its inability
572 to diffuse and be sorbed onto the surface of Mn oxides (Liang et al., 2021b). The waterlogged
573 conditions in this region may facilitate such diffusion and promote the sorption of Cr (III) onto Mn
574 oxides. Meanwhile, the neutral pH conditions prevalent in this area contribute to a negatively charged
575 surface of Mn oxides, enhancing the adsorption of trivalent Cr (e.g., Cr^{3+}, $[CrOH]^{2+}$), thus the
576 possibility for Cr (III) to be oxidized. However, in Ferralsols derived from ultramafic rocks in Brazil,
577 it has been shown that the Cr (VI) generated through the oxidation of Mn oxides may subsequently
578 adsorb onto the soil matrix (i.e. Fe oxides) and be chemically extractable by KH_2PO_4. Therefore, this
579 portion of highly mobile Cr (VI), associated with fine Fe oxide particles, may be transported via post-
580 rainfall runoff, potentially causing harmful environmental effects (Garnier et al., 2013). Such a process
581 cannot be ruled out in our surrounding soils giving the instability of Fe oxides, coupled with the
582 reactivity of Mn oxides. Thus, the toxicity and mobility of Cr (VI) underscore potential environmental
583 threats, particularly concerning groundwater. Therefore, further studies, including KH_2PO_4 extraction
584 of Cr (VI), dissolution studies of FMNs vs. surrounding soils, and particularly those employing
585 synchrotron XAS (X-ray absorption spectroscopy) to examine the speciation of Cr, Mn, and Fe, will
586 provide more precise information regarding valence, or speciation. This will greatly enhance our
587 understanding and interpretation of Cr isotope variations and the cycling of chromium within the soil
588 profile.

589 **5. Conclusions**

590 This study represents the first integration of CBD extraction experiments and chromium isotope
591 techniques to investigate the dynamics, redistribution, and chromium isotopic fractionation within
592 FMNs-rich red soil profiles in southwest China, including non-paddy and paddy soil profiles. The
593 chromium isotope characteristics of soil nodules, a distinctive soil fraction, are also presented for the
594 first time. Our results show that Cr in the red soils is primarily of geogenic origin, deriving from the
595 weathering of the colluvium parent minerals. The effect of land use (non-paddy vs. paddy) is modest
596 on the distribution and/or mobility of Cr within the red soils. FMNs of varying sizes consistently
597 exhibit higher Cr concentrations compared to the surrounding soils, along with more positive $\delta^{53}Cr$
598 values and are considered as pedological archives not reactive to current physicochemical conditions.

Iron oxide extraction technique shows that both FMNs and surrounding soils consistently exhibit heavier signatures in the oxide than in the residual fraction. It suggests the significant capture of isotopically heavy Cr (VI) from soil solution by Fe oxides. Additional variability of $\delta^{53}Cr$ observed in the amorphous iron oxides recently precipitated in an active paddy soil demonstrates the dominant control of soil hydrology on driving the soil redox conditions and thus Cr other redox-sensitive element dynamics. Contrary to FMNs, which are supposed relatively stable under current physicochemical conditions, the long-term persistence of amorphous iron phases in red soils is more questionable. These findings underscore the potential of chromium isotopes as a tool for tracing chromium dynamics within natural soil systems, particularly those abundant in redox features. However, they also indicate that considerable variations in chromium isotope features resulting from these redox processes might obscure information regarding chromium pollution sources. Nonetheless, conducting further investigations, encompassing dissolution experiments, chromium speciation in soil solutions, analysis of chromium isotope characteristics, and acquiring in-situ data on chromium and iron speciation using synchrotron analysis, will significantly enhance our understanding of soil chromium stability and dynamics. Addressing the absence of chromium content and isotope characteristics in vegetation, especially in crops like rice plants, emerges as a crucial avenue for future investigation. Overcoming this limitation will significantly bolster our ability to provide a more direct and comprehensive response to regional food security concerns related to chromium. To achieve this, forthcoming studies could focus on extensive sampling and analysis of chromium content and isotopic signatures in various plant species, particularly those prevalent in regions with heightened chromium exposure. Additionally, conducting controlled greenhouse experiments or field studies aimed at elucidating chromium uptake, translocation, and accumulation mechanisms within plant tissues will be pivotal. These future endeavors hold the promise of shedding light on the role of vegetation as a potential indicator and reservoir of chromium contamination, thereby contributing significantly to strategies aimed at mitigating environmental and agricultural implications linked to chromium pollution.

Acknowledgements

This work was supported by the French National Program EC2CO (Ecosphère Continentale et Côtière). Parts of this work were supported by IPGP multidisciplinary program PARI, and by Paris–

IdF region SESAME Grant no. 12015908. This study contributes to the IdEx Université de Paris ANR-18-IDEX-0001. Mrs Qin work was supported by a China scholarship Council grant that covered her salary in France. We are grateful for Mrs Sophie Nowak help to interpret the XRD data. We thank Pr. F. Moynier for providing the Cr double spike standard. Authors thank three anonymous reviewers for their appreciated comments who improved the quality of this manuscript.

References

Aide, M., 2005. Elemental composition of soil nodules from two alfisols on an alluvial terrace in Missouri. Soil Sci 170, 1022–1033. https://doi.org/10.1097/01.ss.0000187351.16740.55

Ao, M., Chen, X., Deng, T., Sun, S., Tang, Y., Morel, J.L., Qiu, R., Wang, S., 2022a. Chromium biogeochemical behaviour in soil-plant systems and remediation strategies: A critical review. J. Hazard. Mater. 424, 127233. https://doi.org/10.1016/j.jhazmat.2021.127233

Ao, M., Sun, S., Deng, T., Zhang, F., Liu, T., Tang, Y., Li, J., Wang, S., Qiu, R., 2022b. Natural source of Cr (VI) in soil: The anoxic oxidation of Cr (III) by Mn oxides. J. Hazard. Mater. 433, 128805. https://doi.org/10.1016/j.jhazmat.2022.128805

Babechuk, M.G., Weimar, N.E., Kleinhanns, I.C., Eroglu, S., Swanner, E.D., Kenny, G.G., Kamber, B.S., Schoenberg, R., 2019. Pervasively anoxic surface conditions at the onset of the Great Oxidation Event: New multi-proxy constraints from the Cooper Lake paleosol. Precambrian Res 323, 126–163. https://doi.org/10.1016/j.precamres.2018.12.029

Becquer, T., Quantin, C., Sicot, M., Boudot, J.P., 2003. Chromium availability in ultramafic soils from New Caledonia. Sci. Total Environ. 301, 251–261. https://doi.org/10.1016/S0048-9697(02)00298-X

Berger, A., Frei, R., 2014. The fate of chromium during tropical weathering: A laterite profile from Central Madagascar. Geoderma 213, 521–532. https://doi.org/10.1016/j.geoderma.2013.09.004

Bonneville, S., Behrends, T., Van Cappellen, P., 2009. Solubility and dissimilatory reduction kinetics of iron (III) oxyhydroxides: A linear free energy relationship. Geochim. Cosmochim. Acta 73, 5273–5282. https://doi.org/10.1016/j.gca.2009.06.006

Braun, J.-J., Pagel, M., Herbilln, A., Rosin, C., 1993. Mobilization and redistribution of REEs and thorium in a syenitic lateritic profile: A mass balance study. Geochim. Cosmochim. Acta 57, 4419–4434. https://doi.org/10.1016/0016-7037(93)90492-F

Butterly, C.R., Baldock, J.A., Tang, C., 2013. The contribution of crop residues to changes in soil pH under field conditions. Plant Soil 366, 185–198. https://doi.org/10.1007/s11104-012-1422-1

Churchman, G.J., Lowe, D.J., Zealand, N., 2012. Alteration, formation, and occurrence of minerals in soils. Handbook of Soil Sciences. 2nd edition. https://hdl.handle.net/10289/9024

Colwyn, D.A., Sheldon, N.D., Maynard, J.B., Gaines, R., Hofmann, A., Wang, X., Gueguen, B., Asael, D., Reinhard, C.T., Planavsky, N.J., 2019. A paleosol record of the evolution of Cr redox cycling and evidence for an increase in atmospheric oxygen during the Neoproterozoic. Geobiology 17, 579–593. https://doi.org/10.1111/gbi.12360

Cornu, S., Cattle, J.A., Samouëlian, A., Laveuf, C., Guilherme, L.R.G., Albéric, P., 2009. Impact of Redox Cycles on Manganese, Iron, Cobalt, and Lead in Nodules. Soil Sci Soc Am J 73, 1231–1241. https://doi.org/10.2136/sssaj2008.0024

Covelo, E.F., Vega, F.A., Andrade, M.L., 2008. Sorption and desorption of Cd, Cr, Cu, Ni, Pb and Zn by a Fibric Histosol and its organo-mineral fraction. J. Hazard. Mater. 159, 342–347. https://doi.org/10.1016/j.jhazmat.2008.02.025

Crowe, S.A., Døssing, L.N., Beukes, N.J., Bau, M., Kruger, S.J., Frei, R., Canfield, D.E., 2013. Atmospheric oxygenation three billion years ago. Nature 501, 535–538. https://doi.org/10.1038/nature12426

D'Arcy, J., Babechuk, M.G., Døssing, L.N., Gaucher, C., Frei, R., 2016. Processes controlling the chromium isotopic composition of river water: Constraints from basaltic river catchments. Geochim. Cosmochim. Acta 186, 296–315. https://doi.org/10.1016/j.gca.2016.04.027

682 Dimos, V., Haralambous, K.J., Malamis, S., 2012. A Review on the Recent Studies for
683 Chromium Species Adsorption on Raw and Modified Natural Minerals. Crit Rev Environ Sci
684 Technol 42, 1977–2016. https://doi.org/10.1080/10643389.2011.574102
685 Ellis, A.S., Johnson, T.M., Bullen, T.D., 2004. Using Chromium Stable Isotope Ratios To
686 Quantify Cr (VI) Reduction: Lack of Sorption Effects. Environ. Sci. Technol. 38, 3604–3607.
687 https://doi.org/10.1021/es0352294
688 Ettler, V., Chren, M., Mihaljevič, M., Drahota, P., Kříbek, B., Veselovský, F., Sracek, O.,
689 Vaněk, A., Penížek, V., Komárek, M., Mapani, B., Kamona, F., 2017. Characterization of Fe-Mn
690 concentric nodules from Luvisol irrigated by mine water in a semi-arid agricultural area.
691 Geoderma 299, 32–42. https://doi.org/10.1016/j.geoderma.2017.03.022
692 Fandeur, D., Juillot, F., Morin, G., Olivi, L., Cognigni, A., Webb, S.M., Ambrosi, J.-P.,
693 Fritsch, E., Guyot, F., Brown, Jr., G.E., 2009. XANES Evidence for Oxidation of Cr (III) to Cr
694 (VI) by Mn-Oxides in a Lateritic Regolith Developed on Serpentinized Ultramafic Rocks of New
695 Caledonia. Environ. Sci. Technol. 43, 7384–7390. https://doi.org/10.1021/es900498r
696 Feng, J., Pei, L., Zhu, X., Ju, J., Gao, S., 2018. Absolute accumulation and isotope
697 fractionation of Si and Fe during dolomite weathering and terra rossa formation. Chem. Geol.
698 496, 43–56. https://doi.org/10.1016/j.chemgeo.2018.08.018
699 Frank, A.B., Klaebe, R.M., Frei, R., 2019. Fractionation Behavior of Chromium Isotopes
700 during the Sorption of Cr (VI) on Kaolin and its Implications for Using Black Shales as a
701 Paleoredox Archive. Geochemistry, Geophys. Geosystems 20, 2290–2302.
702 https://doi.org/10.1029/2019GC008284
703 Fu, Y., Li, F., Guo, S., Zhao, M., 2021. Cadmium concentration and its typical input and
704 output fluxes in agricultural soil downstream of a heavy metal sewage irrigation area. J. Hazard.
705 Mater. 412, 125203. https://doi.org/10.1016/j.jhazmat.2021.125203
706 Gao, T., Ke, S., Wang, S.J., Li, F., Liu, C., Lei, J., Liao, C., Wu, F., 2018. Contrasting Mg
707 isotopic compositions between Fe-Mn nodules and surrounding soils: Accumulation of light Mg
708 isotopes by Mg-depleted clay minerals and Fe oxides. Geochim. Cosmochim. Acta 237, 205–222.
709 https://doi.org/10.1016/j.gca.2018.06.028

Gao, T., Liu, Yuhui, Xia, Y., Zhu, J.M., Wang, Z., Qi, M., Liu, Yizhang, Ning, Z., Wu, Q., Xu, W., Liu, C., 2021. Cadmium isotope compositions of Fe-Mn nodules and surrounding soils: Implications for tracing Cd sources. Fundam. Res. 1, 269–276. https://doi.org/10.1016/j.fmre.2021.04.002

Garnier, J., Quantin, C., Guimarães, E.M., Vantelon, D., Montargès-Pelletier, E., Becquer, T., 2013. Cr (VI) genesis and dynamics in Ferralsols developed from ultramafic rocks: The case of Niquelândia, Brazil. Geoderma 193–194, 256–264. https://doi.org/10.1016/j.geoderma.2012.08.031

Garnier, J., Quantin, C., Martins, E.S., Becquer, T., 2006. Solid speciation and availability of chromium in ultramafic soils from Niquelândia, Brazil. J Geochem Explor 88, 206–209. https://doi.org/10.1016/j.gexplo.2005.08.040

Gee, G.W., Bauder, J.W., 2018. Particle-size Analysis. pp. 383–411. https://doi.org/10.2136/sssabookser5.1.2ed.c15

Gillman, G.P., Bruce, R.C., Davey, B.G., Kimble, J.M., Searle, P.L., Skjemstad, J.O., 1983. A comparison of methods used for determination of cation exchange capacity. Commun Soil Sci Plant Anal 14, 1005–1014. https://doi.org/10.1080/00103628309367428

Grossman, R.B., Reinsch, T.G., 2018. 2.1 Bulk Density and Linear Extensibility. pp. 201–228. https://doi.org/10.2136/sssabookser5.4.c9

Guinoiseau, D., Fekiacova, Z., Allard, T., Druhan, J.L., Balan, E., Bouchez, J., 2021. Tropical Weathering History Recorded in the Silicon Isotopes of Lateritic Weathering Profiles. Geophys. Res. Lett. 48. https://doi.org/10.1029/2021GL092957

Hai, J., Liu, L., Tan, W., Hao, R., Qiu, G., 2020. Catalytic oxidation and adsorption of Cr (III) on iron-manganese nodules under oxic conditions. J. Hazard. Mater. 390, 122166. https://doi.org/10.1016/j.jhazmat.2020.122166

He, Z., Zhang, M., Wilson, M.J., 2004. Distribution and Classification of Red Soils in China, in: The Red Soils of China. Springer Netherlands, Dordrecht, pp. 29–33. https://doi.org/10.1007/978-1-4020-2138-1_3

Holmgren, G.G.S., 1967. A Rapid Citrate-Dithionite Extractable Iron Procedure. Soil Sci

738 Soc Am J 31, 210–211. https://doi.org/10.2136/sssaj1967.03615995003100020020x
739 Huang, Y., Wang, L., Wang, W., Li, T., He, Z., Yang, X., 2019. Current status of agricultural
740 soil pollution by heavy metals in China: A meta-analysis. Sci. Total Environ. 651, 3034–3042.
741 https://doi.org/10.1016/j.scitotenv.2018.10.185
742 Johnston, C.P., Chrysochoou, M., 2014. Mechanisms of chromate adsorption on hematite.
743 Geochim. Cosmochim. Acta 138, 146–157. https://doi.org/10.1016/j.gca.2014.04.030
744 Kok, J.F., Adebiyi, A.A., Albani, S., Balkanski, Y., Checa-Garcia, R., Chin, M., Colarco, P.R.,
745 Hamilton, D.S., Huang, Y., Ito, A., Klose, M., Leung, D.M., Li, L., Mahowald, N.M., Miller, R.L.,
746 Obiso, V., Pérez García-Pando, C., Rocha-Lima, A., Wan, J.S., Whicker, C.A., 2021. Improved
747 representation of the global dust cycle using observational constraints on dust properties and
748 abundance. Atmospheric Chem. Phys. 21, 8127–8167. https://doi.org/10.5194/acp-21-8127-2021
749 Larsen, K.K., Wielandt, D., Schiller, M., Bizzarro, M., 2016. Chromatographic speciation of
750 Cr (III)-species, inter-species equilibrium isotope fractionation and improved chemical
751 purification strategies for high-precision isotope analysis. J. Chromatogr. A 1443, 162–174.
752 https://doi.org/10.1016/j.chroma.2016.03.040
753 Li, D., Li, G., He, Y., Zhao, Y., Miao, Q., Zhang, H., Yuan, Y., Zhang, D., 2022. Key Cr
754 species controlling Cr stability in contaminated soils before and chemical stabilization at a
755 remediation engineering site. J. Hazard. Mater. 424, 127532.
756 https://doi.org/10.1016/j.jhazmat.2021.127532
757 Liang, C., Fu, F., Tang, B., 2021a. Mn-incorporated ferrihydrite for Cr (VI) immobilization:
758 Adsorption behavior and the fate of Cr (VI) during aging. J. Hazard. Mater. 417, 126073.
759 https://doi.org/10.1016/j.jhazmat.2021.126073
760 Liang, J., Huang, X., Yan, J., Li, Y., Zhao, Z., Liu, Y., Ye, J., Wei, Y., 2021b. A review of the
761 formation of Cr (VI) via Cr (III) oxidation in soils and groundwater. Sci. Total Environ. 774,
762 145762. https://doi.org/10.1016/j.scitotenv.2021.145762
763 Liu, C., Xu, L., Liu, C., Liu, J., Qin, L., Zhang, Z., Liu, S., Li, S., 2019. High□Precision
764 Measurement of Stable Cr Isotopes in Geological Reference Materials by a Double□Spike TIMS
765 Method. Geostand Geoanal Res 43, 647–661. https://doi.org/10.1111/ggr.12283

766 Lutterotti, L., Matthies, S., Wenk, Hjin., others, 1999. MAUD: a friendly Java program for
767 material analysis using diffraction. IUCR Newsl. CPD 21, 14–15.
768 Mänd, K., Planavsky, N.J., Porter, S.M., Robbins, L.J., Wang, C., Kreitsmann, T., Paiste, K.,
769 Paiste, P., Romashkin, A.E., Deines, Y.E., Kirsimäe, K., Lepland, A., Konhauser, K.O., 2022.
770 Chromium evidence for protracted oxygenation during the Paleoproterozoic. Earth Planet. Sci.
771 Lett. 584, 117501. https://doi.org/10.1016/j.epsl.2022.117501
772 Nelson, D.W., Sommers, L.E., 2015. Total Carbon, Organic Carbon, and Organic Matter. pp.
773 539–579. https://doi.org/10.2134/agronmonogr9.2.2ed.c29
774 Pai, C.W., Wang, M.K., Chiang, H.C., King, H.B., Hwong, J.-L., Hu, H.T., 2003. Formation
775 of iron nodules in a Hapludult of central Taiwan. Can J Soil Sci 83, 167–172.
776 https://doi.org/10.4141/S02-068
777 Paulukat, C., Døssing, L.N., Mondal, S.K., Voegelin, A.R., Frei, R., 2015. Oxidative release
778 of chromium from Archean ultramafic rocks, its transport and environmental impact - A Cr
779 isotope perspective on the Sukinda valley ore district (Orissa, India). Appl. Geochemistry 59,
780 125–138. https://doi.org/10.1016/j.apgeochem.2015.04.016
781 Qin, L., Wang, X., 2017. Chromium isotope geochemistry, in: Non-Traditional Stable
782 Isotopes. Rev Mineral Geochem 82, 379–414. https://doi.org/10.2138/rmg.2017.82.10
783 Quantin, C., Becquer, T., Rouiller, J.H., Berthelin, J., 2002. Redistribution of Metals in a
784 New Caledonia Ferralsol After Microbial Weathering. Soil Sci Soc Am J 66, 1797–1804.
785 https://doi.org/10.2136/sssaj2002.1797
786 Rauch, J.N., Pacyna, J.M., 2009. Earth's global Ag, Al, Cr, Cu, Fe, Ni, Pb, and Zn cycles.
787 Global Biogeochem Cycles 23, 1–16. https://doi.org/10.1029/2008GB003376
788 Ren, S., Song, C., Ye, S., Cheng, C., Gao, P., 2022. The spatiotemporal variation in heavy
789 metals in China's farmland soil over the past 20 years: A meta-analysis. Sci. Total Environ. 806,
790 150322. https://doi.org/10.1016/j.scitotenv.2021.150322
791 Rosales-Landeros, C., Barrera-Díaz, C.E., Bilyeu, B., Guerrero, V.V., Núñez, F.U., 2013. A
792 Review on Cr(VI) Adsorption Using Inorganic Materials. Am. J. Anal. Chem. 04, 8–16.
793 https://doi.org/10.4236/ajac.2013.47A002

Roy, K.S., Bhattacharyya, P., Neogi, S., Rao, K.S., Adhya, T.K., 2012. Combined effect of elevated CO2 and temperature on dry matter production, net assimilation rate, C and N allocations in tropical rice (Oryza sativa L.). Field Crops Res. 139, 71–79. https://doi.org/10.1016/j.fcr.2012.10.011

Rudnick, R.L., Gao, S., 2014. Composition of the Continental Crust, in: Treatise on Geochemistry, Second Ed., pp. 1–51. https://doi.org/10.1016/B978-0-08-095975-7.00301-6

Shaheen, S.M., Rinklebe, J., 2014. Geochemical fractions of chromium, copper, and zinc and their vertical distribution in floodplain soil profiles along the Central Elbe River, Germany. Geoderma 228–229, 142–159. https://doi.org/10.1016/j.geoderma.2013.10.012

Shahid, M., Shamshad, S., Rafiq, M., Khalid, S., Bibi, I., Niazi, N.K., Dumat, C., Rashid, M.I., 2017. Chromium speciation, bioavailability, uptake, toxicity and detoxification in soil-plant system: A review. Chemosphere 178, 513–533. https://doi.org/10.1016/j.chemosphere.2017.03.074

Sipos, P., Kovács, I., Barna, G., Tóth, A., Makó, A., Palcsu, L., Kiss, G., Horváth, A., Puskás-Preszner, A., 2023. Iron isotope fractionation during the formation of ferromanganese nodules under different conditions of hydromorphism. Geoderma 430, 116286. https://doi.org/10.1016/j.geoderma.2022.116286

Sossi, P.A., Moynier, F., van Zuilen, K., 2018. Volatile loss following cooling and accretion of the Moon revealed by chromium isotopes. Proc. Natl. Acad. Sci. U.S.A. 115, 10920–10925. https://doi.org/10.1073/pnas.1809060115

Sun, S.S., Ao, M., Geng, K.R., Chen, J.Q., Deng, T.H.B., Li, J.J., Guan, Z.T., Mo, B.L., Liu, T., Yang, W.J., Tang, Y.T., Qiu, R.L., 2022. Enrichment and speciation of chromium during basalt weathering: Insights from variably weathered profiles in the Leizhou Peninsula, South China. Sci. Total Environ. 822, 153304. https://doi.org/10.1016/j.scitotenv.2022.153304

Sun, Z., Wang, X., Planavsky, N., 2019. Cr isotope systematics in the Connecticut River estuary. Chem. Geol. 506, 29–39. https://doi.org/10.1016/j.chemgeo.2018.12.034

Thomas, G.W., 2018. Soil pH and Soil Acidity. pp. 475–490. https://doi.org/10.2136/sssabookser5.3.c16

Wang, L., Jin, Y., Weiss, D.J., Schleicher, N.J., Wilcke, W., Wu, L., Guo, Q., Chen, J., O'Connor, D., Hou, D., 2021. Possible application of stable isotope compositions for the identification of metal sources in soil. J. Hazard. Mater. 407, 124812. https://doi.org/10.1016/j.jhazmat.2020.124812

Wang, M., Chen, W., Peng, C., 2016. Risk assessment of Cd polluted paddy soils in the industrial and township areas in Hunan, Southern China. Chemosphere 144, 346–351. https://doi.org/10.1016/j.chemosphere.2015.09.001

Wang, Z., Wen, Y., Gou, W., Ji, J., Li, W., 2023. Zn isotope signatures in soil Fe Mn nodules with karst high geochemical background. Sci. Total Environ. 882, 163365. https://doi.org/10.1016/j.scitotenv.2023.163365

Wei, W., Klaebe, R., Ling, H.-F., Huang, F., Frei, R., 2020. Biogeochemical cycle of chromium isotopes at the modern Earth's surface and its applications as a paleo-environment proxy. Chem. Geol. 541, 119570. https://doi.org/10.1016/j.chemgeo.2020.119570

Wei, X., Hao, M., Shao, M., Gale, W.J., 2006. Changes in soil properties and the availability of soil micronutrients after 18 years of cropping and fertilization. Soil Tillage Res 91, 120–130. https://doi.org/10.1016/j.still.2005.11.009

Wei, X., Ji, H., Wang, S., Chu, H., Song, C., 2014. The formation of representative lateritic weathering covers in south-central Guangxi (southern China). Catena (Amst) 118, 55–72. https://doi.org/10.1016/j.catena.2014.01.019

Wille, M., Babechuk, M.G., Kleinhanns, I.C., Stegmaier, J., Suhr, N., Widdowson, M., Kamber, B.S., Schoenberg, R., 2018. Silicon and chromium stable isotopic systematics during basalt weathering and lateritisation: A comparison of variably weathered basalt profiles in the Deccan Traps, India. Geoderma 314, 190–204. https://doi.org/10.1016/j.geoderma.2017.10.051

Wu, G., Zhu, J.-M., Wang, X., Johnson, T.M., Han, G., 2020. High-Sensitivity Measurement of Cr Isotopes by Double Spike MC-ICP-MS at the 10 ng Level. Anal. Chem. 92, 1463–1469. https://doi.org/10.1021/acs.analchem.9b04704

Xiao, G., Hu, Y., Li, N., Yang, D., 2018. Spatial autocorrelation analysis of monitoring data of heavy metals in rice in China. Food Control 89, 32–37.

https://doi.org/10.1016/j.foodcont.2018.01.032

Yang, L., 2006. The physical and chemic characters of ferromanganese nodules in the quaternary red earth in southern China (Master thesis). Zhejiang Normal University. (in Chinese)

Yang, Q., Yang, Z., Zhang, Q., Liu, X., Zhuo, X., Wu, T., Wang, L., Wei, X., Ji, J., 2021. Ecological risk assessment of Cd and other heavy metals in soil-rice system in the karst areas with high geochemical background of Guangxi, China. Sci. China Earth Sci. 64, 1126–1139. https://doi.org/10.1007/s11430-020-9763-0

Yu, G., Fu, F., Ye, C., Tang, B., 2020. Behaviors and fate of adsorbed Cr (VI) during Fe (II) -induced transformation of ferrihydrite-humic acid co-precipitates. J. Hazard. Mater. 392, 122272. https://doi.org/10.1016/j.jhazmat.2020.122272

Yu, X., Wang, Y., Zhou, G., Peng, G., Brookes, P.C., Lu, S., 2020. Paleoclimatic fingerprints of ferromanganese nodules in subtropical Chinese soils identified by synchrotron radiation-based microprobes. Chem. Geol. 531, 119357. https://doi.org/10.1016/j.chemgeo.2019.119357

Zhang, K., Yang, Y., Chi, W., Chen, G., Du, Y., Hu, S., Li, F., Liu, T., 2023. Chromium transformation driven by iron redox cycling in basalt-derived paddy soil with high geological background values. J Environ Sci (China) 125, 470–479. https://doi.org/10.1016/j.jes.2021.12.013

Zhang, L., Fu, F., Yu, G., Sun, G., Tang, B., 2022. Fate of Cr (VI) during aging of ferrihydrite-humic acid co-precipitates: Comparative studies of structurally incorporated Al (III) and Mn (II). Sci. Total Environ. 807, 151073. https://doi.org/10.1016/j.scitotenv.2021.151073

Zhang, M., Wilson, M.J., He, Z., 2004. Mineralogy of Red Soils in Southern China in Relation to Their Development and Charge Characteristics, in: The Red Soils of China. Springer Netherlands, Dordrecht, pp. 35–61. https://doi.org/10.1007/978-1-4020-2138-1_4

Zhu, J., Wu, G., Wang, X., Han, G., Zhang, L., 2018. An improved method of Cr purification for high precision measurement of Cr isotopes by double spike MC-ICP-MS. J Anal At Spectrom 33, 809–821. https://doi.org/10.1039/C8JA00033F

Zhu, K., Sossi, P.A., Siebert, J., Moynier, F., 2019. Tracking the volatile and magmatic history of Vesta from chromium stable isotope variations in eucrite and diogenite meteorites.

878 Geochim. Cosmochim. Acta 266, 598–610. https://doi.org/10.1016/j.gca.2019.07.043
879

Table 1

Soil key physicochemical properties.

Profile	Horizon	pH	SOM	Density	CEC	Clay	Slit	Sand	FMNs distribution				ba*
									> 5 mm	2-5 mm	1-2 mm	Total	
			g/kg	g/cm^3	cmol/kg	%			g/kg bulk				
Wangling Non-paddy	A	4.9	30.9	1.5	12.4	37.5	23.2	39.3	177	500	82	759	0.02
	B	4.7	19.8	1.7	17.8	40.0	22.5	37.5	87	613	55	755	0.02
Wangling Paddy	Ap1	6.2	49.7	1.3	15.0	34.0	32.4	33.6	81	262	61	404	0.05
	Ap2	7.3	37.9	1.6	14.9	23.0	39.9	37.1	108	310	45	463	0.05
	AB	7.3	16.9	1.7	11.8	23.0	31.4	45.6	124	334	47	506	0.04
	Br1	7.4	12.0	1.5	21.1	33.0	27.9	39.1	59	264	53	376	0.04
	Br2	7.2	8.4	1.2	20.1	37.0	27.4	35.6	42	231	101	374	0.04
Litang Non-paddy	A	7.0	25.7	1.4	12.0	16.0	33.9	50.1	124	411	75	610	0.07
	AB	7.1	26.5	2.0	15.5	39.0	27.2	33.8	274	421	26	721	0.05
	B	7.4	15.4	1.7	16.5	36.0	27.5	36.5	254	403	25	681	0.06
Litang Paddy	Ap1	6.5	50.3	0.9	15.3	28.0	51.0	21.0	15	36	3	55	0.19
	Ap2	7.3	31.1	1.5	15.9	25.0	51.9	23.1	11	28	5	44	0.19
	AB	7.4	16.6	1.8	20.5	35.0	41.7	23.3	10	33	4	47	0.16
	Brg	7.1	12.7	1.7	23.4	39.0	38.4	22.6	35	107	17	158	0.12
	Br	7.2	6.7	2.3	24.1	39.0	24.4	36.6	124	291	36	451	0.09

*ba: the soil-weathered eluviation coefficient. FMNs: iron-manganese nodules.

Table 2

Element and Cr isotope compositions of irrigation waters, rocks, and fertilizers.

Element		Irrigation water		Rock			Fertilizer						
		Wangling	Litang	Carbonate1	Carbonate2	Calcite	F0 (NPK 45%, 15-15-15)	F1 (NPK 51%, 17-17-17)	F2 (NPK 45%, 15-15-15)	F3 (NPK 45%, 15-15-15)	F4 (NPK 45%, 15-15-15)	F5 (NPK 45%, 15-15-15)	F6 (NPK 30%, 18-5-7)
δ^{53}Cr ± 2SD	‰	1.47 ± 0.06	0.16 ± 0.02	1.30 ± 0.07	0.72 ± 0.04	1.01 ± 0.03	0.34 ± 0.01	0.33 ± 0.07	0.36 ± 0.04	1.49 ± 0.12	0.44 ± 0.04	0.11 ± 0.03	0.45 ± 0.04
P	g/kg	bdl	0.001	bdl	bdl	0.002	66.9	72.4	62.5	75.5	62.6	70.1	18.2
K		0.004	0.02	0.003	0.01	0.01	127.7	139.0	133.0	118.9	128.0	117.2	55.9
Ca		0.06	0.06	395.9	395.3	209.5	7.6	8.7	8.8	1.8	9.3	11.4	8.9
Mn		bdl	0.001	2.7	2.7	16.2	724.1	400.7	574.2	88.1	421.0	162.4	100.6
Fe		bdl	0.002	46.8	45.2	175.6	7026.5	4149.2	5323.7	796.8	4353.3	2121.4	2238.3
Cr	μg/kg (ug/L for water samples)	0.07	0.28	3876.8	3836.2	4037.6	19980.5	22300.5	21552.7	8862.1	23074.1	16408.4	25792.8

bdl=blow detection limit.

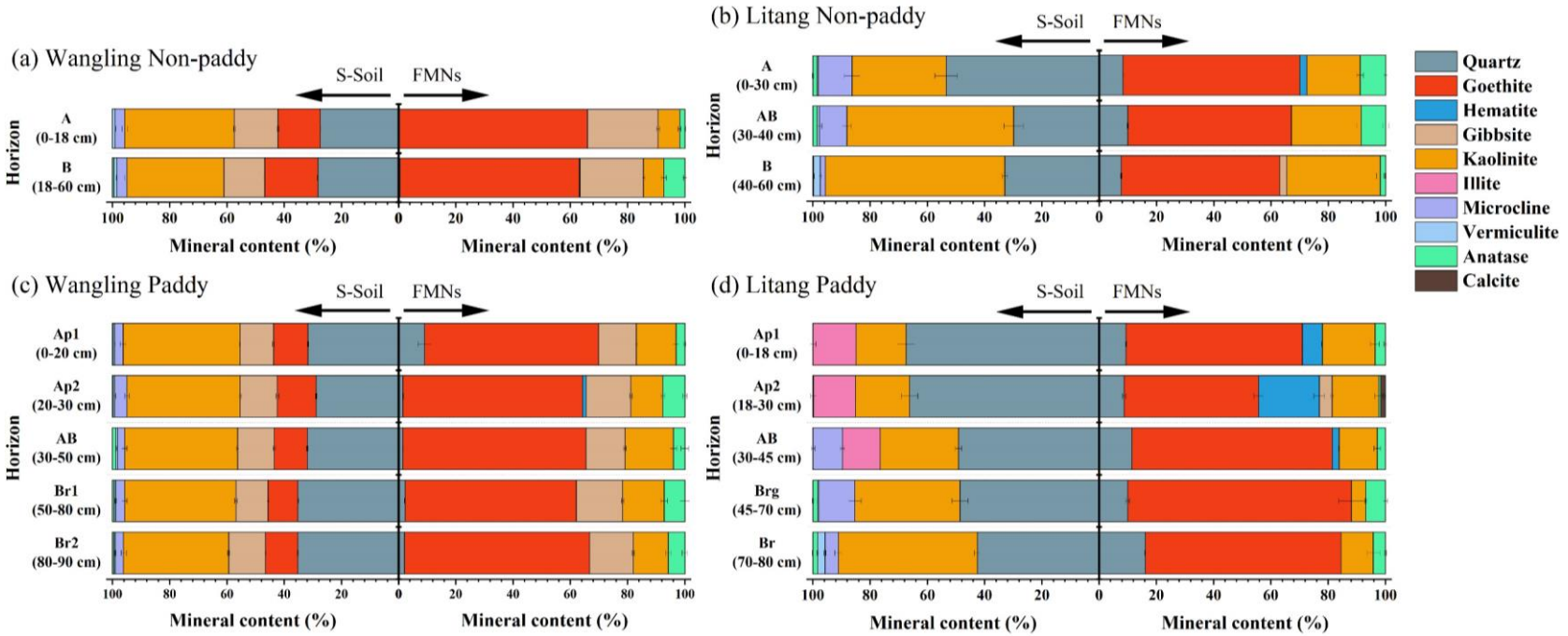

Fig. 1. Variations in mineral content obtained by XRD analysis of the surrounding soils and FMNs (bulk of all sizes) in non-paddy and paddy profiles of Wangling and Litang. S-Soil: surrounding soil, FMNs: iron-manganese nodules.

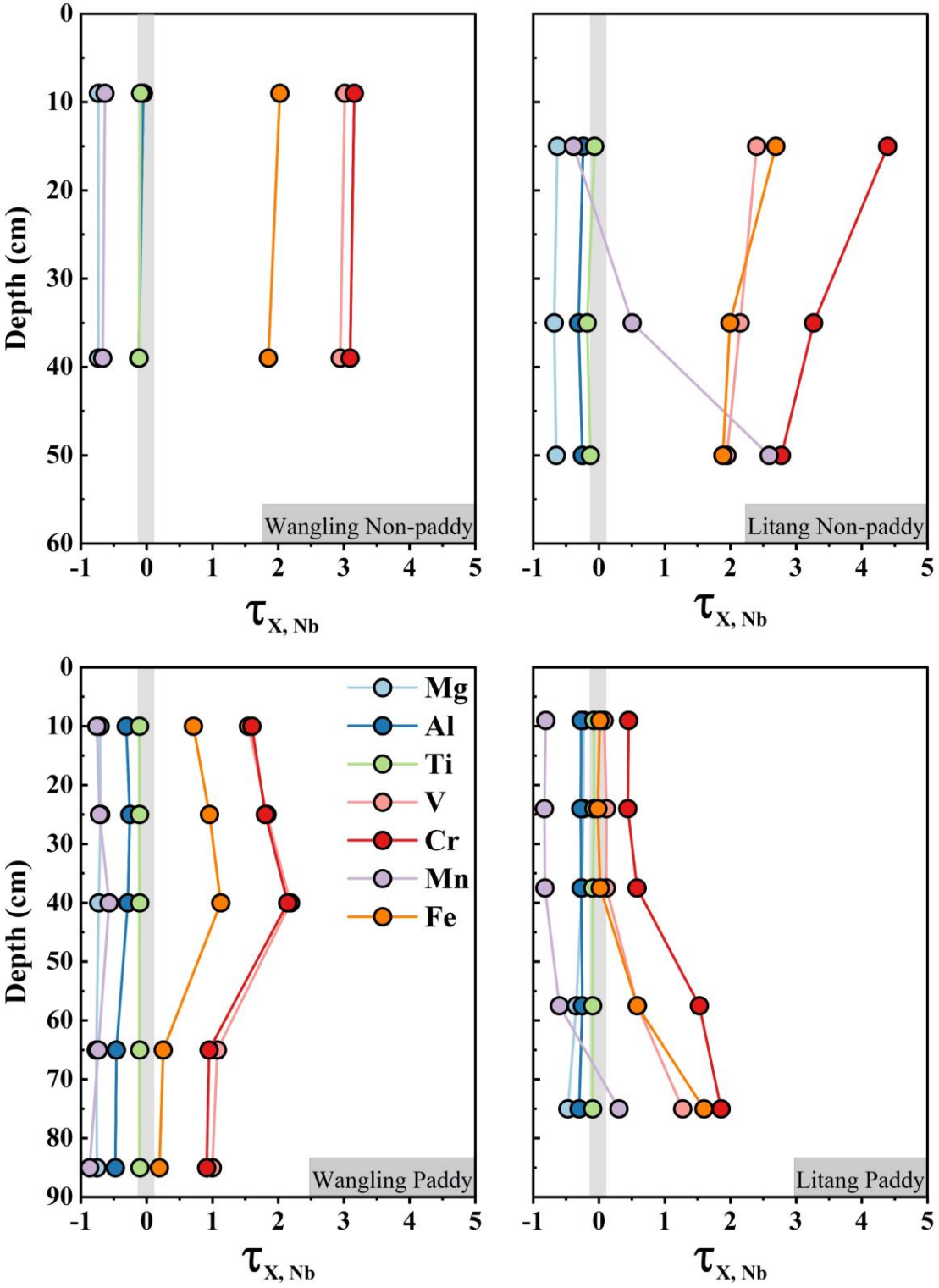

Fig. 2. Key element mass balance coefficients ($\tau_{X,Nb}$) in the non-paddy and paddy soil profiles of Wangling and Litang.

10

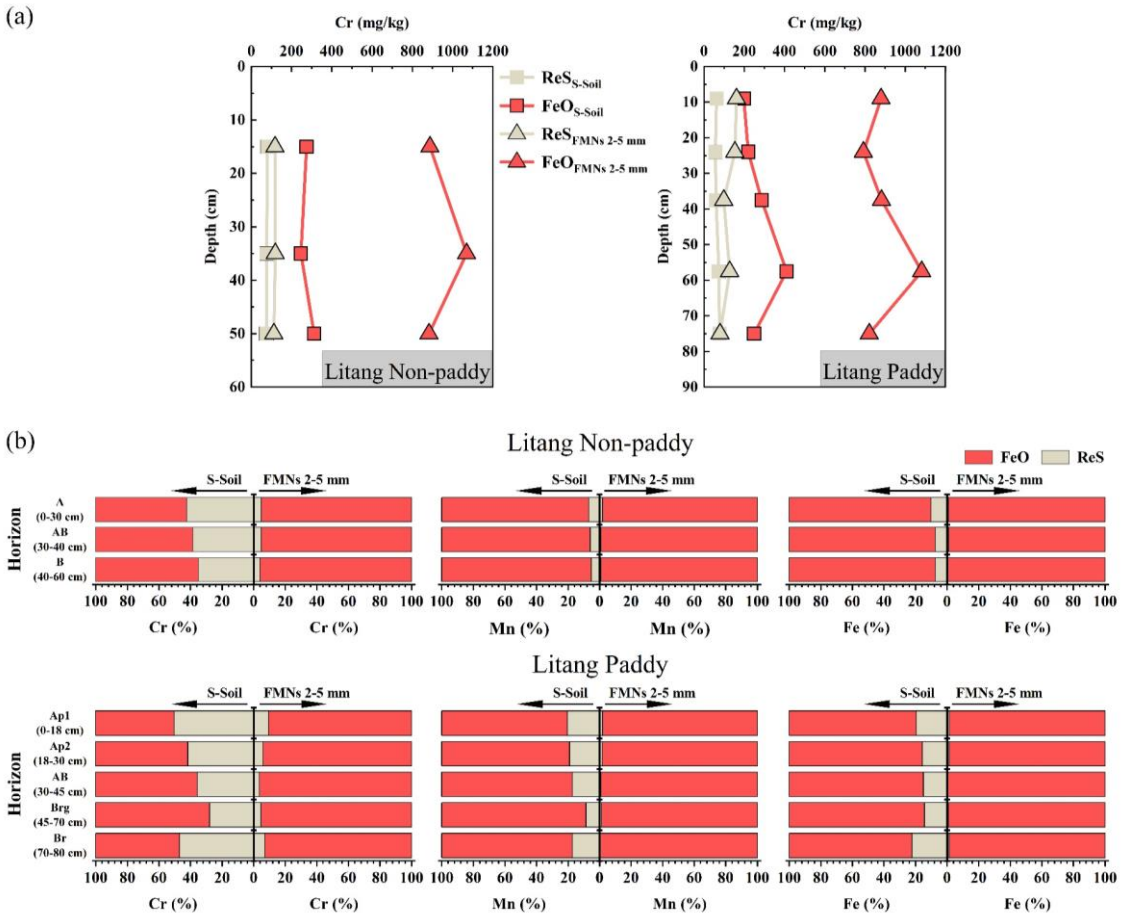

11

12 Fig. 3. CBD extraction results of (a) Cr concentrations of residue (ReS) and extract (FeO). (b)
13 Relative distributions of Cr, Mn, and Fe between ReS and FeO in the surrounding soils and FMNs 2-
14 5 mm in Litang soil profiles. S-Soil: surrounding soil, FMNs: iron-manganese nodules.

15

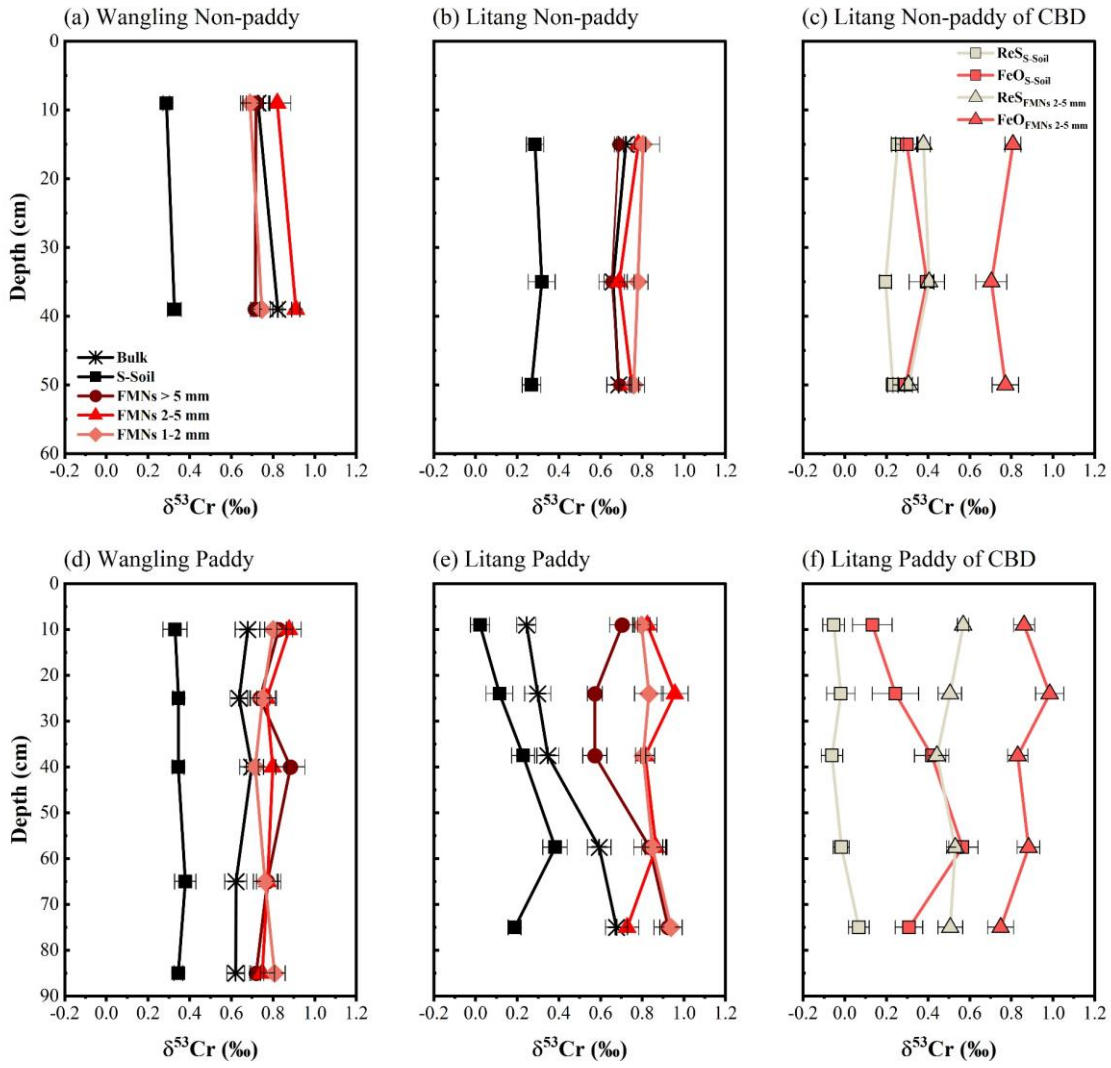

Fig. 4. Chromium isotope composition of samples in non-paddy and paddy profiles of Wangling, Litang before and after CBD extraction. Bulk: the bulk soil containing FMNs and surrounding soil, S-Soil: surrounding soil, FMNs: iron-manganese nodules, ReS and FeO: the residue and extract of CBD extraction, respectively. The error bars show the 2SD uncertainty derived from repeat measurements.

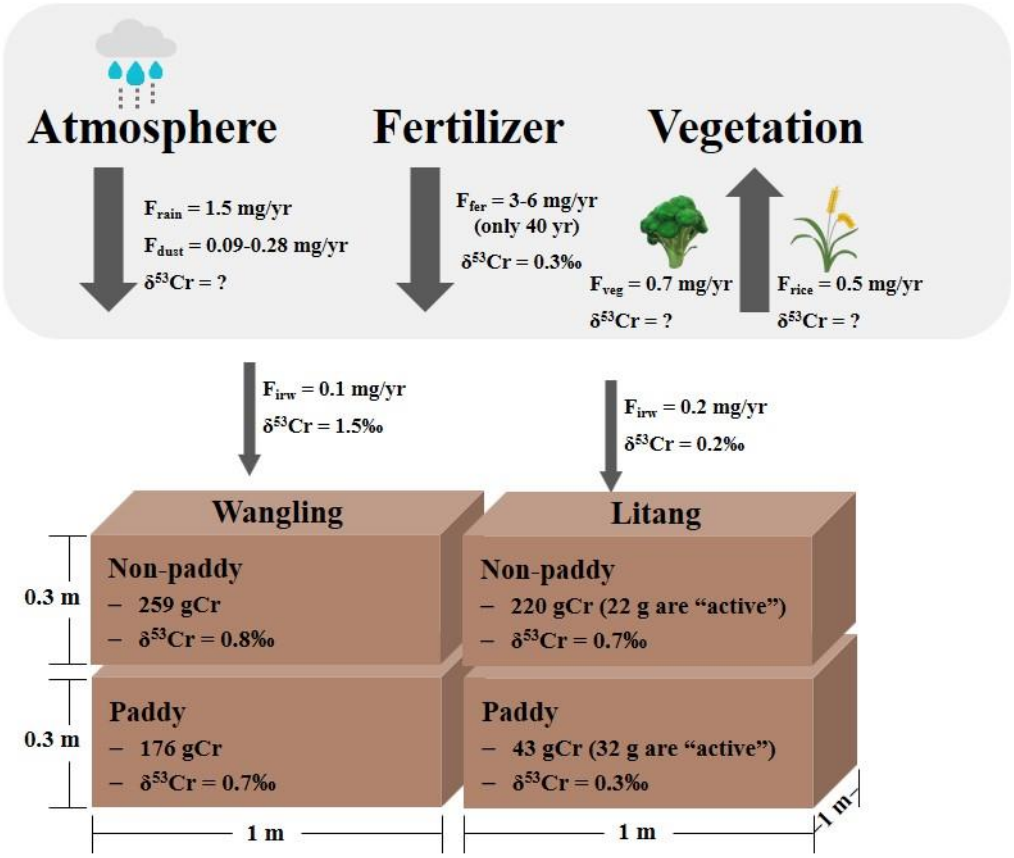

Fig. 5. Fluxes and stocks of Cr in the soil profiles of cultivated soil horizon in 0.3 m^3 box at Wangling and Litang. F_{rain}: rainwater Cr flux, F_{dust}: human-derived dust Cr flux, F_{fer}: fertilizer Cr flux, F_{veg}: vegetable Cr flux in non-paddy field, F_{rice}: rice Cr flux in paddy field, F_{irw}: irrigation water Cr flux.

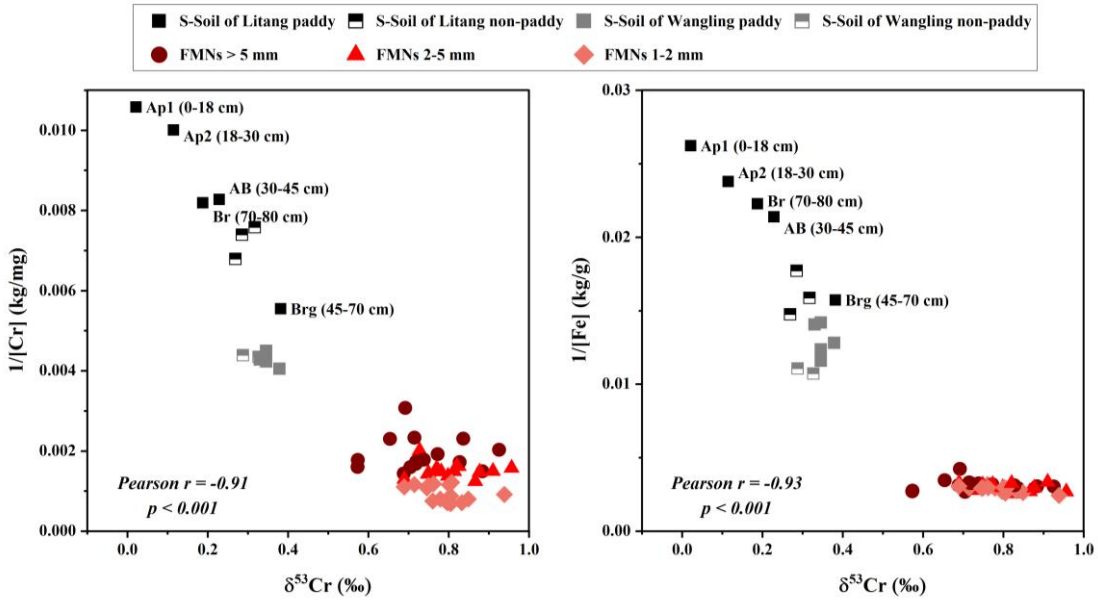

Fig. 6. $\delta^{53}Cr$ values vs 1/[Cr] and 1/[Fe] of the surrounding soils and FMNs of different sizes in Wangling and Litang. S-Soil: surrounding soil, FMNs: iron-manganese nodules.

Environmental Implication

The existence of iron-manganese nodules (FMNs) in soil plays a crucial role in addressing soil pollution, especially when it comes to heavy metals. Our research demonstrates that FMNs found in red soils effectively capture and secure substantial quantities of the more easily movable and harmful form of chromium called Cr (VI), which also happens to be heavier in terms of its isotopic properties. This mainly happens because of the dominant presence of iron oxide in FMNs. This process significantly lowers the risk of chromium contamination in the red soils of the area we studied. Nevertheless, it's essential to stress the importance of further investigation into how stable these non-crystalline forms of iron oxide-bound chromium are in the surrounding soils over a long period.

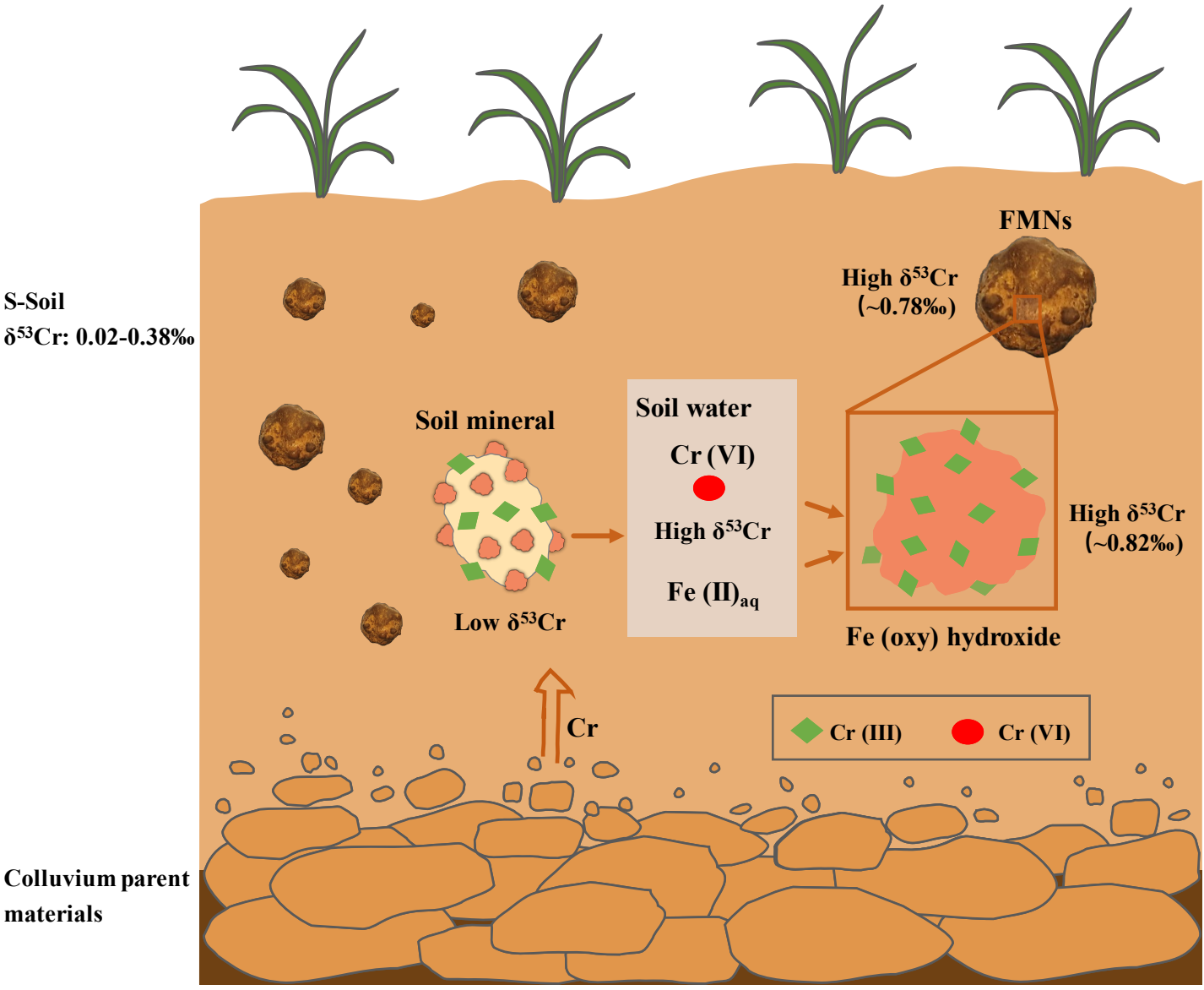
S-Soil
δ53Cr: 0.02-0.38‰
FMNs
High δ53Cr
(~0.78‰)
Soil mineral
Soil water
Cr (VI)
High δ53Cr
Fe (II)aq
High δ53Cr
(~0.82‰)
Low δ53Cr
Fe (oxy) hydroxide
Cr
Cr (III)
Cr (VI)
Colluvium parent
materials

Highlights

- Cr isotope data in soil FMNs is reported for the first time.
- FMNs/Fe oxides capture isotopically heavy Cr (VI).
- Redox and not land use drives Fe oxide formation and FMNs, affecting Cr mobility.
- Cr in red soil profiles mainly results from colluvium mineral weathering.